Research and Development of Segmented Secondary Emission Beam Monitors for J-PARC Neutrino Beamline

Kodai Yamada
Department of Physics, University of Tokyo

January 31, 2007

Abstract

We develop a Segmented Secondary Emission Monitor (SSEM) as a beam profile monitor for the T2K experiment. The T2K experiment is a next generation long baseline neutrino oscillation experiment, based on the high intensity narrow band neutrino beam produced by the high intensity and high power primary proton beam in the J-PARC proton synchrotron accelerator. To handle the high power proton beam, precise and stable beam control is required. SSEM measures the beam size as well as position of the primary proton beam. The requirements for SSEM are the beam size resolution of better than 3.5%, the beam position resolution of ~ 0.25mm, long term gain stability, radiation hardness, to equip with a moving mechanism (~ 0.1mm positioning accuracy) and the proper performance under cryogenic temperature of ~ 80K. We design SSEM to satisfy the above requirements. To check the performance, the beam test in the KEK PS line, cryogenic tests, irradiation tests and simulation studies are carried out. We confirm that our design satisfies the requirements. We also design the specification of signal readout devices and confirm the sufficient performance of the prototype.

Contents

Chapter 1

Introduction

In 1998, Super-Kamiokande discovered the existence of neutrino oscillation in the atmospheric neutrinos[1]. Neutrino oscillation occurs among the three " flavors " of neutrinos if neutrinos have non-zero mass and mixing. Under these circumstances, flavor states are mixtures of mass states, and a neutrino may change its apparent flavor with time. Neutrino masses were assumed to be zero in the current Standard Model, proposed in the 1970s to describe the fundamental forces and elementary particles. The discovery of neutrino oscillations and hence non-zero neutrino masses requires a theory beyond the Standard Model, and the apparent smallness of the neutrino masses indicates physics with a large energy scale.

To confirm the neutrino oscillation phenomena and to more precisely determine the fundamental neutrino oscillation parameters of mass differences and mixing angles, several accelerator-based long baseline neutrino oscillation experiments have been carried out. The experiments use the accelerator-based neutrino beams as controlled and high-flux sources of neutrinos. The accelerator-based neutrino beams allow direct measurement of the neutrino flux near the source, followed by another measurement after the beam traverses the baseline. Measurement of the change in the flux of a particular neutrino type enables us to determine parameters of neutrino oscillation.

The first accelerator-based long baseline neutrino oscillation experiment, K2K (KEK to Kamioka), was carried out from 1999 to 2005, and obtained the evidence for the oscillation [2]. Following the K2K, MINOS experiment with the Fermilab NuMI beam has been carried out. The first results of the MINOS were presented in 2006 [3], and reported the consistent results with Super-K and K2K experiments [4].

The T2K (Tokai to Kamioka) neutrino experiment [5, 6] is the next generation long baseline neutrino experiment in Japan. One feature of the experiment is a high intensity narrow band neutrino beam that is produced by a high intensity and high power proton synchrotron (PS) at J-PARC,. The beam power of J-PARC PS is nearly 100 times more than that of KEK 12GeV PS, which was a neutrino source for the K2K experiment. The high power J-PARC proton beam results in a high intensity neutrino beam that is 50 times more intense than K2K beam. Such a high intensity neutrino beam provides a plenty statistics for a precise measurement of the neutrino oscillation. The other feature of the experiment is an off axis beam (OAB) configuration to produce the narrow neutrino energy spectrum to maximize the neutrino oscillation at the far detector.

The J-PARC neutrino beam line is under construction. The proton beam extracted from the J-PARC PS is bent and dumped onto a carbon graphite target to produce neutrinos. The primary beam line equips with superconducting magnets to bend the beam. To avoid quenching the superconducting magnets and destructing the target by such a high intensity beam, a precise beam control is required. For this purpose, various beam monitors are planned to be installed. A Segmented Secondary Emission Monitor (SSEM) is developed as a profile monitor. If the incident proton beam transverses segmented thin metal strips, secondary electrons are emitted and compensating charge flows into the strips. The measured charge amount on each strip enables to reconstruct the incident beam profile. The simple structure and the simple principle are advantage of this monitor against the stressful and low-accessible environment of J-PARC.

In this thesis, we report the R&D status of SSEM for the T2K experiment. To check the SSEM performance, the beam test in the KEK PS line, cryogenic tests, irradiation tests and simulation studies are carried out. We confirm that our design satisfies the requirements for the T2K experiment. We also design the specification of signal readout devices and confirm the sufficient performance of the prototype.

The motivation of the R&D is described in Chapter 2, the mechanical details of the SSEM components in Chapter 3, the readout system for SSEM in Chapter 4, the performance study using a test beam in Chapter 5, and the simulation study in Chapter 6. Finally, Chapter 7 summarizes the thesis.

Chapter 2

Motivation of the R&D

In this chapter, we briefly introduce the T2K neutrino oscillation experiment (Section 2.1) and focus on the J-PARC neutrino beamline, which is a specially designed proton beamline to produce a high intensity narrow band neutrino beam (Section 2.2). The main role of the neutrino beamline is to bend the proton beam with superconducting magnets and bump the beam to the carbon graphite target. For the proper beam delivery along the beamline, a precise beam control is required. For this purpose, various beam monitors have been developed. A profile monitor, Segmented Secondary Emission Monitor (SSEM), is one of them, and this thesis concerns SSEM.

The aim of this chapter is to describe the function of SSEM and summarize requirements.

2.1 T2K experiment

2.1.1 Physics motivation

The main physics motivation of the T2K neutrino experiment is to explore physics at energy scale much higheer than the electro-weak unification energy scale. Neutrino mass and mixing can be one of a few possible windows of physics near the Grand Unification energy scale. In addition, comparison of neutrino and anti-neutrino oscillations can be the only possible way to search for leptonic CP violation. The T2K project aims to study of physics beyond the Standard Model through precision measurements of the masses and mixing of leptons, which seem to be very different from those of quarks.

Neutrino oscillation

The neutrino oscillation probability relevant to the experiment can be approximetly expressed by the following formula:

$$P(\nu_\mu \to \nu_\mu) \sim 1 - \sin^2 2\theta_{23} \sin^2 \Theta_{23}, \tag{2.1}$$

$$P(\nu_\mu \to \nu_e) \sim \frac{1}{2} \sin^2 2\theta_{13} \sin^2 \Theta_{23}. \tag{2.2}$$

where

$$\Theta_{23} = 1.27\Delta m^2_{23}[\mathrm{eV}^2]L[\mathrm{km}]/E_\nu[\mathrm{GeV}] \tag{2.3}$$

gives oscillation pattern depending on the flight length L and the neutrino energy E_ν. Δm^2_{23} is one of the mass square differences. The indices 2 and 3 in Δm^2_{23} are indices of the mass eigenstates. An experimental constraint obtained from ν_μ disappearance in the atmospheric neutrino is $1.6 \times 10^{-3} < \Delta m^2_{23} < 4 \times 10^{-3}\mathrm{eV}^2$ [7].

Goals of the experiment

The goals of this experiment at the first stage are:

- Discovery of $\nu_\mu \to \nu_e$ oscillation at $\Delta m^2 \sim 3 \times 10^{-3}\mathrm{eV}^2$ down to $\sin^2 2\theta_{13} \sim 0.006$. This is a factor of twenty improvements in sensitivity over the past experiment,
- Precise measurement of the oscillation parameters in ν_μ disappearance down to $\delta(\Delta m^2) = 10^{-4}\mathrm{eV}^2$ and $\delta(\sin^2 2\theta_{23}) = 0.01$, and
- Search for a sterile component in ν_μ disappearance by the neutral current events measurement.

If these goals are successfully achieved, we further proceed to the second stage of the experiment. In the second stage, CP violation in the lepton sector will be investigated with the upgraded accelerator (5 times more power) and with the 1Mt Hyper-Kamiokande (20 times larger in size than SK).

2.1.2 Overview of the experiment

The T2K experiment is a next generation long baseline neutrino oscillation experiment following the K2K experiment, in Japan. In T2K, a muon neutrino beam is produced at the J-PARC 50GeV proton synchrotron in Tokai, and is detected by the Super-Kamiokande in Kamioka (See Figure 2.1). The baseline length is about 295km. The PS is designed to deliver 3.3×10^{14} protons every 3.4 seconds (0.77MW). This corresponds to 50 times higher intensity and more than 100 times higher beam power than those for KEK-PS. Accordingly the neutrino beam has higher intensity and it provides more precise measurements of the neutrino oscillation parameters than the K2K results. A feature of the T2K experiment is its high intensity narrow band neutrino beam. The neutrino energy is tunable with off-axis configuration (described below), and the well-defined energy spectrum has an advantage to achieve the maximum sensitivity for neutrino oscillation. The peak of the neutrino energy will be tuned to ~ 0.8GeV, which maximizes the neutrino oscillation amplitude based on Eq. 2.3. L in the equation is the baseline length of 295km in the T2K experiment. Indeed, Θ_{23} is about $\pi/2$ at $\Delta m^2_{23} = 3 \times 10^{-3}$, $L = 295$ and $E_\nu = 0.8$GeV.

Neutrino beam

A neutrino beam is produced with a conventional method. A proton beam is bombarded to the target to produce pions. Then, a muon neutrino beam is produced via the pion decays.

To obtain a narrow neutrino energy spectrum, we adopt an off axis beam (OAB) configuration. In the OAB method, the neutrino detectors are placed at a few degrees (Off-Axis angle) off from the beam axis as shown in Figure 2.2.

Since pion decay is a two-body decay, the neutrino energy from the parent pion is the constant at the pion's rest frame. With a finite decay angle, the neutrino energy, therefore,

Figure 2.1: Overview of the T2K experiment

becomes insensitive to the parent pion momentum as shown in Figure 2.3 and equation,

$$E_\nu = \frac{m_\pi^2 - m_\mu^2}{2\left(E_\pi - p_\pi \cos\theta\right)} \sim \frac{E_\pi\left(m_\pi^2 - m_\mu^2\right)}{m_\pi^2 + p_\pi^2 \sin^2\theta}. \tag{2.4}$$

The peak energy of the neutrino spectrum is set to about 0.8GeV by choosing the off axis angle (2 to 3 degrees).

The advantages of the narrow neutrino energy spectrum are,

- to reduce the inelastic interactions of the high energy tail neutrinos which are misidentified as charged current quasi elastic (CCQE) events,
- to reduce π_0 productions which are the major background to electron neutrino events, and
- to reduce the systematic error of the pion production uncertainty.

Adopting the OAB configuration, the total neutrino flux decreases, but the high power proton beam compensates the loss.

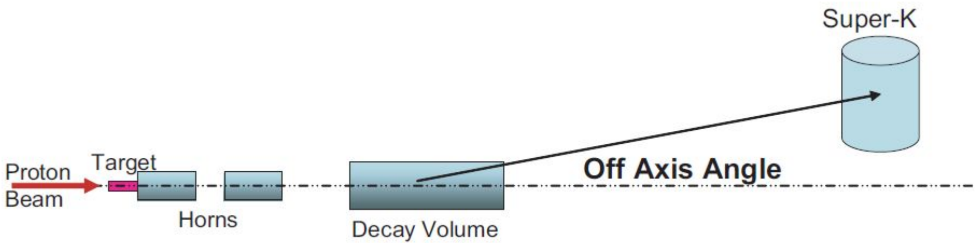

Figure 2.2: Overview of the off axis beam

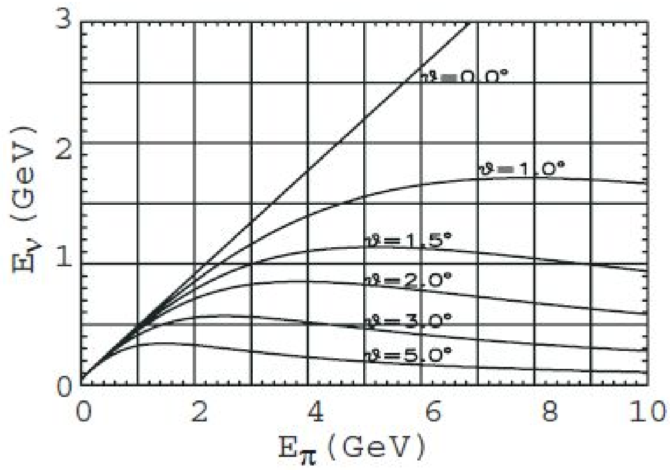

Figure 2.3: Energy distribution of neutrino at some off-axis angle

J-PARC accelerator and fast extraction

The layout of the J-PARC facility is shown in Figure 2.4. The J-PARC accelerator consists of the 400MeV Linac, the 3GeV Synchrotron (RCS:Rapid Cycling Synchrotron), and the 50GeV Synchrotron (50GeV-PS). In the 50GeV-PS, the expected intensity of the proton beam is 3.3×10^{14}ppp (protons per pulse) and the repetition rate is about 0.3Hz.The proton beam consists of 8 bunches and the bunch time interval is about $\sim$ 600nsec. Finally, the beam is extracted to the neutrino beamline keeping the bunch structure and transported to the neutrino production target, which is made of graphite (3cm in diameter and 90cm in length). This extraction scheme is called "fast extraction". The specifications of the KEK-PS and the J-PARC PS are summarized in Table 2.1.

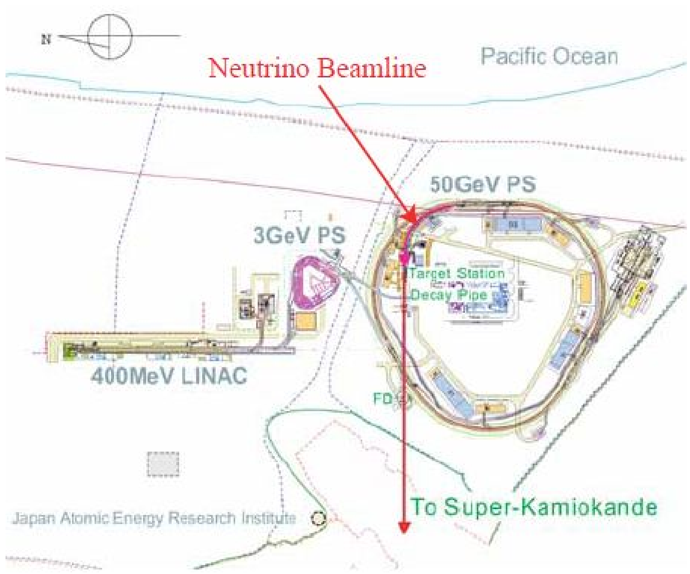

Figure 2.4: Overview of the JPARC accelerator

	KEK PS	J-PARC PS
Beam Energy (GeV)	12	30
Beam Intensity (ppp)	6.6×10^{12}	3.3×10^{14}
Repetition Rate (Hz)	0.46	0.28
Spill width (μsec)	1.1	5
# of bunches	9	8
Bunch width (nsec)	50	50-60
Beam Power (MW)	0.0052	0.75

Table 2.1: Comparison of the proton accelerators for the neutrino experiments.

Neutrino beamline

The proton beam extracted from the 50GeV PS to the neutrino beamline is bent by about 80 degrees toward Kamioka and transported to the target. The proton beam hits the target and produces a number of pions and kaons by the hadronic interaction. The produced pions and kaons are focused toward SK by three toroidal horn magnets. In the horns, the positive charged hadrons are focused and the negative ones are spread. The pions and kaons decay into muons and muon neutrinos in the decay volume. After the decay volume, an iron and concrete beam dump stop all charged particles except high energy muons. The direction and the intensity of the muons are measured by a muon monitor.

Near neutrino detector

The produced neutrino beam is measured by the near neutrino detectors at 280m downstream from the target. One is set at the off axis degrees, and the other is set on axis of the proton beam. The purpose of these detectors is to measure the stability of neutrino beam direction, total flux and energy spectrum. In addition, electron neutrino contamination will be measured.

At the 280m detector, the shape of the neutrino spectrum is different from that at Super-K; the decay pipe, which is the neutrino source, has a finite length and, therefore, it can be seen as an extended source at 280m away from the target. At Super-K, the geometrical effect of the decay pipe is negligible and it can be seen as a point source. Then, another detector (intermediate detector) is being considered at 2km form the target. Spectrum at the intermediate detector is predicted to be very similar to that at SK.

Super Kamiokande

The Super-Kamiokande (Super-K) is used as the far detector in the T2K experiment.

The detector is the 50,000 ton Water Cerenkov detector constructed under the mountain at Kamioka. Its performance and results for atmospheric neutrinos and solar neutrinos are written elsewhere [1, 8, 9].

The schematic view of the detector is shown in Figure 2.5. The detector cavern is 42m in height and 39m in diameter. There is an inner detector surrounded by an outer detector. The inner detector has 11146, 50cmϕ PMTs and the outer detector has 1885, 20cmϕ PMTs. The PMTs of the inner detector detects Cerenkov photon rings by relativistic charged particles which are produced by the interaction of neutrinos. The aim of the outer detector is to veto the charged particles from the outside of Super-K. The detector is very sensitive for sub-GeV neutrinos and has superb e/μ identification capability.

Interactions of neutrinos from the accelerator are identified by synchronizing the timing between the beam extraction time at the accelerator and the trigger time at Super-K using GPS. The synchronization accuracy of the two sites will be better than 200nsec as in the K2K experiment. The typical accidental coincidence rate of atmospheric neutrino events is negligibly small than the signal rate of about $\times 10^{-3}$/spill in the T2K experiment.

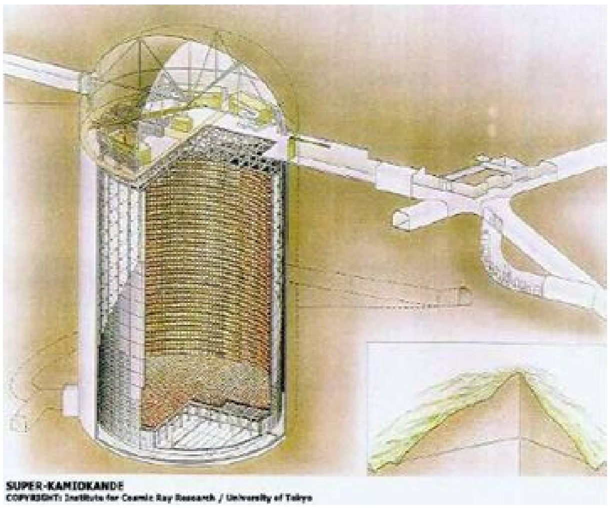

Figure 2.5: Overview of the Super Kamiokande detector

2.2 J-PARC neutrino beamline

In this desction, we describe a primary proton beam portion of the J-PARC neutirno beamline. This beamline instrumentation includes magnets, beam position and profile monitors and collimators. Using these components, we deliver the proton beam extracted from the 50GeV PS to the target with minimum loss. We describe the beam monitors and the beam tuning scheme for the beam transportation. In particular, we describe in detail the beam profile monitors.

2.2.1 Beam monitors

We plan to install four kinds of beam monitors to the primary proton beamline: position monitors, intensity monitors, profile monitors and loss monitors. We briefly describe these monitors.

Position monitor

The position monitor measures the beam center position. As the position monitor, Electro Static Monitor (ESM) has been developed. Four electrodes are attached on the inner wall of upper, lower, right and left sides of the beam duct. The electrical potential induced by the proton beam is measured. The signal asymmetries of upper and lower electrodes, and right and left electrodes are calculated, which are converted to the beam positions in the horizontal and vertical directions, respectively. The merits of the monitor are: the structure is very simple, the signal size is large, and this monitor is non-destructive. It also has a potential to provide the beam size information.

Profile monitor

The profile monitor measures the beam profile that is the beam shape and position. As the profile monitor, we have developed a Segmented Secondary Emission Monitor (SSEM). When the incident proton beam transverses segmented thin metal strips, secondary electrons are emitted and compensating charge flows into the strips. The amount of charge on each strip enables to reconstruct the incident beam profile. This technique is used in many accelerators and beamlines [14, 15, 16, 17]. The simple principle and the simple structure are important advantages of this monitor. On the other hand, it is a destructive monitor that interferes with the beam. This will cause the large beam loss and will also cause the aging of the monitor itself. This disadvantage limits the monitor usage in the full intensity operation.

At K2K, SPIC (gas-chamber) is used as the position and profile monitor. SPIC is also a destructive profile monitor, the structure of which is more complicated than that of SSEM.

We studied another type of monitor, Residual Gas Beam Profile Monitor (RGBPM) with Micro Channel Plate (MCP), as a candidate of the beam profile monitor. This monitor has been developed as a "non-destructive" profile monitor to always monitor the beam profile in front of the target [12]. This monitor uses the ionization of residual gas, which induced by the incident beam. Both electrons and ions produced by the ionization can be potentially used for the profile measurement. However, the preceding experiment [12] has indicated that RGBPM is not expected to work under the J-PARC environment. According to the report, if we use the electrons as signal, there is too large background noise induced by the beam to measure the profile. If we use the ions, which are detected with a sufficient delay from the background, the high electric field induced by the high intensity beam distorts the profile. In both cases, we cannot measure the proper beam profile by RGBPM in the J-PARC neutrino beamline. Thus, we have decided to use OTR in front of the target.

Intensity monitor

The intensity monitor measures the beam intensity. As the intensity monitor, Current Transformer (CT) has been developed. The electromagnetic induction due to the proton beam is measured, and the signal is proportional to the beam intensity. This technique had been already used in the K2K neutrino beamline. The device is non-destructive to the beam.

Loss monitor

To measure the beam loss, an ion chamber has been developed. High voltage is applied to the coaxial metal tube into which air is poured, and the air ionized by the charged particles is collected and read out. The signal is proportional to the beam loss. The beam loss monitor will be installed around the beam duct every few meters along the beamline.

Complementarity of ESM and SSEM

The profile monitor we have chosen, SSEM, can also be used as a position monitor by extracting the beam position from the measured beam profile. In the low intensity operation, therefore, both SSEM and ESM can be used for the position measurement. The advantages and disadvantages of each monitor are summarized in Table 2.2. SSEM provides visible information of the beam status more directly (that is, destructively). The error of the measured beam position, however, depends on the beam size. In fact, we have confirmed that the beam position accuracy becomes worse for the larger beam size (see, Chapter 6). In addition, the moving mechanism can deteriorate the absolute positioning accuracy. On the other hand, ESM cannot provide the direct information but can provide the constant position resolution and the reliable absolute positioning accuracy with the simple attachment structure. Using these monitors complementarily enables us to do a cross check for the beam position measurement and to monitor the long term age deterioration of ESM. The ESM behavior may gradually change because ESM is exposed to the beam even in the full intensity operation. For this check, a SSEM and a ESM will be installed as a pair.

	Visible information	Position accuracy	
		Mesurement accuracy	Absolute accuracy
SSEM	Yes	Dependence on the beam size	Worry about the moving mechanism
ESM	No	Constant	Reliance with the simple attachment structure

Table 2.2: Comparison between SSEM and ESM as a position monitor .

2.2.2 Beam tuning scheme and function of profile monitors

To transport the beam to the target, we must tune magnets precisely along the beamline. We describe the tuning scheme here.

At J-PARC, the beam intensity is too high to compromise the beamline components. We, therefore, plan to use two different beam intensities for the beam tuning, full intensity and 1/100 of the full intensity. The full intensity corresponds to the maximum intensity of 3.3×10^{12}ppp. The 1/100 intensity is the intensity decreased to 1% keeping the bunch structure. The 1/100 intensity beam is primarily used for the beam tuning because it is less damaging to the beamline components. We increase the intensity up to the full intensity after the beam tuning. In the increasing process, however, it is possible that the beam optics may slightly change. Thus, the short check of the beam status in the full intensity operation may be necessary. SSEM is exposed during the beam tuing, and so SSEM is not used for the physics run (full intensity).

The primary proton beamline consists of three sections: the preparation section, the arc section and the final focusing section as shown in Figure 2.6. The preparation section regulates the extracted proton beam to protect the beamline components in the arc section. The arc section bends the proton beam by about 80 degrees with superconducting magnets. The final focusing section adjusts the beam size to the target size and bends the beam downward to Kamioka.

The beam information required by the tuning is collected by various monitors, especially, ESM and SSEM. For example, the beam path is measured by both ESM and SSEM, and beam parameters including the beam emittance are measured by SSEM.

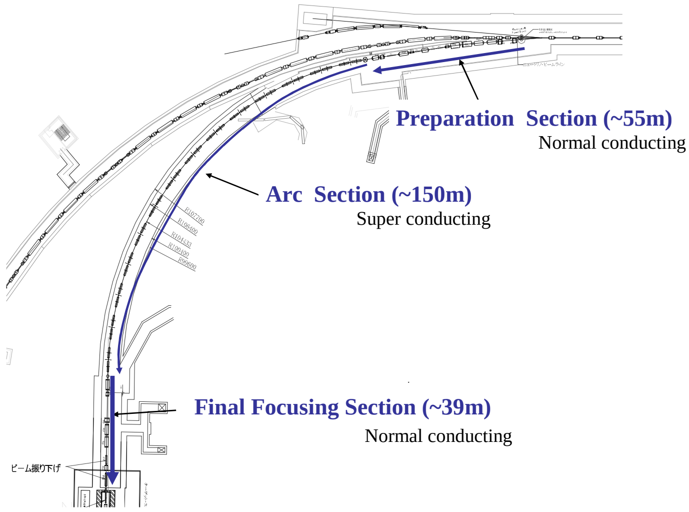

Figure 2.6: Overview of the J-PARC neutrino beamline

Preparation section (prep section)

The preparation section consists of normal conducting magnets, various beam monitors and collimators. In this section, it is important to protect the arc section. If the beam size is too large in the arc section, it is possible for the beam to damage the beamline components and to quench the superconducting magnet. To achieve the protection, the precise beam parameters, α and β of twiss parameters and ϵ(emittance), at the entrance of the beamline (initial beam parameters) must be known because we extrapolate the beam parameters in the arc section using inital parameters and check whether the parameters are suitable or not.

We plan to install 9 SSEMs in the prep. section. The beam profiles measured by these monitors are used to specify the initial beam parameters and to check the beam path. This is the main function of the profile monitors in the prep. section.

Arc section

The arc section consists of superconducting combined function (CF) magnets, a few steering magnets and the beam monitors. The aim of this section is to bend the proton beam by about 80 degrees toward Kamioka. The CF magnet has dipole and quadrupole magnetic fields in one magnet. This is advantage of saving space and cost. However, this has a disadvantage of inflexibility for the beam tuning because this magnet does not allow one to change the current.

We plan to install at least 4 SSEMs in the arc section. The main function of these monitors is to check the beam path and spread.

Final focusing section (FF section)

The final focusing section consists of normal conducting magnets and beam monitors. This section adjusts the beam size to the target size and bends the beam vertically downward to Kamioka with the off-axis angle. One of the critical issues is to protect the target. If the beam size is too narrow or the beam position is too far from the ideal one, inhomogeneous heating can break the target. To avoid the target destruction, we must precisely extrapolate the beam parameters at the target.

We plan to install 5 SSEMs in the FF. section. The beam profiles measured by these monitors are used to estimate the beam parameters at the target and to check the beam path. This is the main function of the profile monitors in the FF. section.

2.2.3 Requirements for profile monitors

In the lights of above, we list requirements for the profile monitors.

The functions of the profile monitors are strongly related to the beam tuning scheme as described above. They are summarized as follows:

- to measure the beam profile precisely enough for us to estimate the beam parameters with acceptable errors,
- to measure the beam path with ESM, and
- to check aging deterioration of ESM.

Several beamline simulations indicate that the beam size accuracy of better than 3.5% is required for the safe beam delivery. The beamline simulations with 0.35mm beam position accuracy have shown the beam delivery. The simualtions have assumed the measurement accuracy of 0.25mm and the absolute positioning accuracy of 0.2mm. It is desired that the SSEM also achieves 0.25mm accuracy. Regarding the third requiement, the position accuracy of 0.25mm is also required because the ESM accuracy is confirmed to be about 0.25mm.

In addition, there remain three requirements. One is radiation hardness since the radiation level in the J-PARC neutrino beamline is very high. In particular, the gain stability of the monitor is important. The monitor must be able to operate at the cryogenic temperature in the arc section because the superconducting magnets are cooled down to the temperature of liquid helium. The surrounding temperature around the monitor is estimated to be $\sim$ 80K. In addition, the precision moving mechanism must be equipped because the SSEM cannot be used in the full intensity operation. The positioning accuracy deterioration by the moving mechanism is desired to be less than 0.1mm.

The requirements for the SSEM are summarized as follows:

- Beam size measurement resolution of better than 3.5%,
- Beam position measurement resolution of $\sim$ 0.25mm,
- Long term gain stability,
- Radiation hardness,
- Need to be equipped with a moving mechanism with 0.1mm positioning accuracy,
- Proper performance under the cryogenic temperature ($\sim$ 80K).

Chapter 3

Overview of SSEM

In the J-PARC neutrino beam line, it is important to control the proton beam precisely using various beam monitors. The profile monitor is one of such monitors as described in the previous chapter. We choose a Segmented Secondary Emission Monitor (SSEM) as the profile monitor. In this chapter, we introduce the principle of SSEM; we describe SSEM for the J-PARC neutrino beam line.

The requirements to be confirmed for SSEM for the J-PARC neutrino beam line are,

- Need to be equipped with moving mechanism with 0.1mm positioning accuracy,
- Radiation hardness, and
- Proper performance under the cryogenic temperature ($\sim$ 80K).

3.1 Principle of SSEM

Figure 3.1 shows a schematic view of SSEM. This monitor consists of anode and cathode electrodes made of thin metal foils. The secondary electrons are emitted when the incident proton beam traverses these electrodes. The number of the secondary electrons is proportional to the intensity of the incident proton beam. According to the former experiments, the secondary emission efficiency is reported to be several percent for the incident charged particles, which are protons or electrons in the energy range of MeV to GeV. The emitted secondary electrons are collected by anode electrodes, and compensating charge which flows into the cathode is read out as a pulse with positive polarity. The compensating charges from the segmented cathode electrodes are read out separately. The measured charges of the each readout channels are proportional to the beam intensity of the strip position and thus we can measure the beam profile.

3.2 Overview of J-PARC SSEM

Figure 3.2 shows a schematic view of the whole SSEM system in the J-PARC neutrino beam line. Main body of SSEM is attached to the moving guide which is fixed inside the chamber. The moving guide is used to insert SSEM into the beam line on demand. To drive the moving mechanism, a stepping motor is attached to the driving shaft outside the chamber, and a motor controller is located in the electronics pit, 80-150m far from

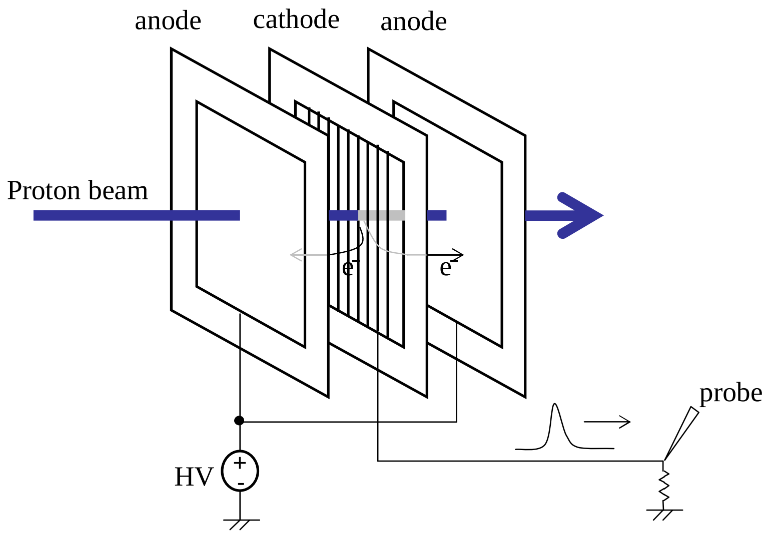

Figure 3.1: Principle of SSEM.

the motor. For signal readout, signal cables are installed between the electrodes and the readout system. These cables consist of many conducting lines to transmit channel-by-channel signal to the readout system. The detailed specification and R&D status of each component are described in the next section.

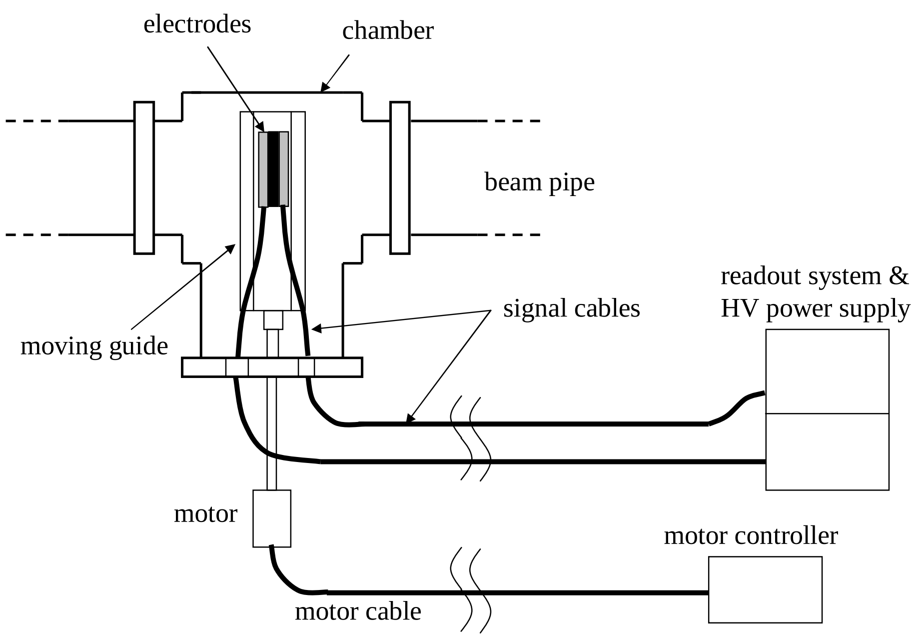

Figure 3.2: Schematic view of SSEM in the J-PARC neutrino beam line.

3.3 Mechanical components of SSEM

SSEM for the J-PARC neutrino beam line consists of various components of electrodes, a vacuum chamber, cables, a moving mechanism, and readout devices. Almost all of them are now under development. We briefly describe the R&D status of them except the readout devices in this section. As for the readout devices, we describe in Chapter 4.

Electrodes

The electrode consists of a frame and a foil (or foils). Figure 3.3 shows a schematic view of a package of the electrodes. There are one anode and two cathodes. About 100volts is applied to the center anode, which absorbs the secondary emitted electrons from cathodes. The two cathodes are set up in two different directions, horizontal and vertical, in order to measure both horizontal and vertical beam profiles at the same time.

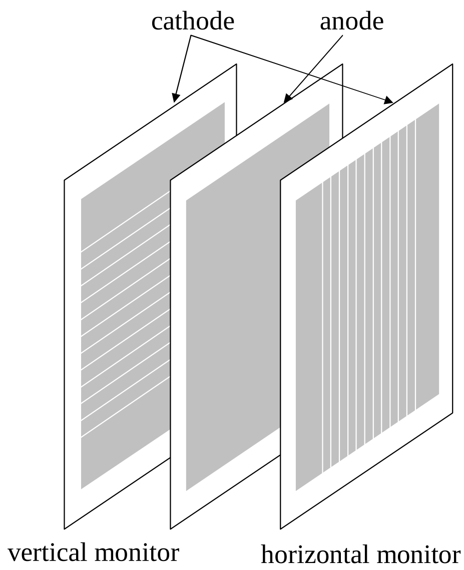

Figure 3.3: Schematic view of a package of electrodes.

As the foils, we chose 5μm thick titanium foils, and fixed the segmentation design of the cathode. The foil material, titanium, is suitable in the J-PARC neutrino beam line in view of the amount of material, the mechanical strength and the melting point [10]. The comparison of the secondary emission efficiency among several materials was also carried out. Figure 3.4 shows the efficiencies normalized by the efficiency of cupper. The black points are the result of the SSEM beam test carried out in the K2K neutrino beamline [10], and the blue points are the result of the 70MeV electron beam experiment performed at SLAC [13]. There exists some discrepancy between the two results. In both cases, however, the efficiency of titanium is confirmed to be several percent, which is sufficient for the J-PARC neutrino beamline. The very thin, 5μm, foils are adopted to suppress the beam loss while keeping signal gain since the beam loss is proportional to the thickness, but the secondary emission gain is proportional not to the thickness but to the surface area.

As for the cathode segmentation, we plan to adopt several different designs different on the beam sizes. Because SSEMs will be installed at various positions along the beam line,

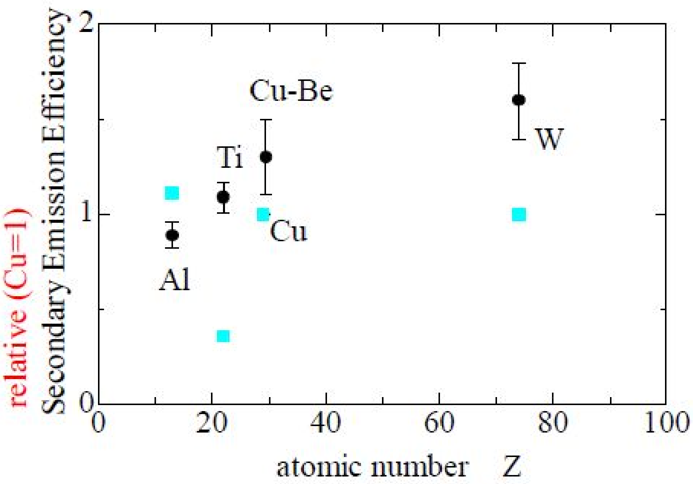

Figure 3.4: Comparison of the secondary emission efficiency among various materials. The black points are the result of the SSEM beam test carried out in the K2K neutrino beamline [10], and the blue points are the result of the 70MeV electron beam experiment performed at SLAC [13].

and must measure the various beam sizes at the positions. Based on the beam optics of the beam line, the range of the beam size is 6-33mm. The design template is determined as shown in Figure 3.5. The cathode mainly consists of 22 strips with the uniform width and spacing. These strips detect the whole beam core. The spacing is fixed to be 1mm. The uniform design is chosen because precise measurement of the edge of the beam core, is important for the extraction of the beam size. In this design template, the strip width is the only parameter to change the SSEM coverage area. Table 3.1 shows the adoption of the strip width, which is determined to let the all monitors in the same beam size range to cover at least double range of the beam size. Validity of this design selection is confirmed by a beam test and a simulation described in Chapter 6. Then, two large strips will be laid at both ends of the cathode as drawn as dotted boxes in Figure 3.5. These strips are placed to detect the beam halo.

Beam size(mm)	Strip width(mm)
< 11	1
< 16.5	2
< 22	3
< 27.5	4
≥ 27.5	5

Table 3.1: Adoption policy of the strip width.

A stainless-steel square frame is developed as the SSEM main flame. The size of the frame is 24cm (20cm) in an outer (inner) side for the prep. and the FF sections, or 17cm (13cm) for the arc section. Figure 3.6 shows a photo of the prototype frame. Stainless-steel

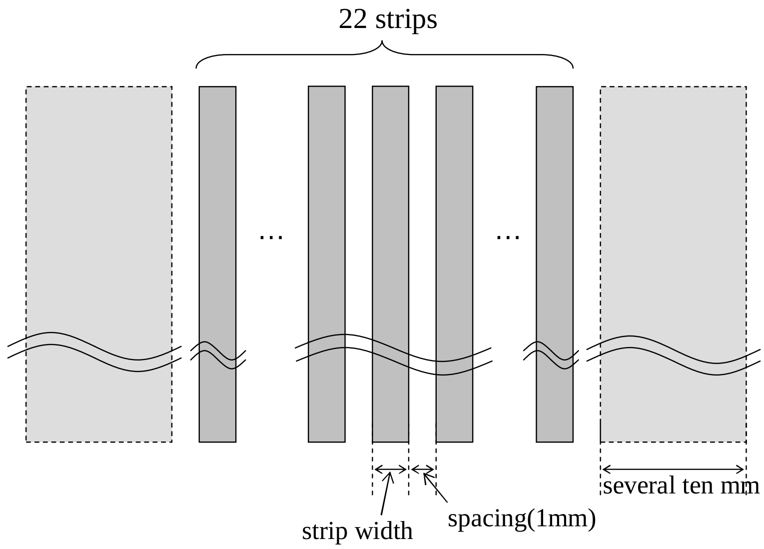

Figure 3.5: Design template of the cathode segmentation.

plates with stoppers are held down to the frame to clump the titanium foils to the frame, which is determined by the acceptance of the beam. For insulation, the polyimide films are inserted between the plate and the foils, and the foils and the frame.

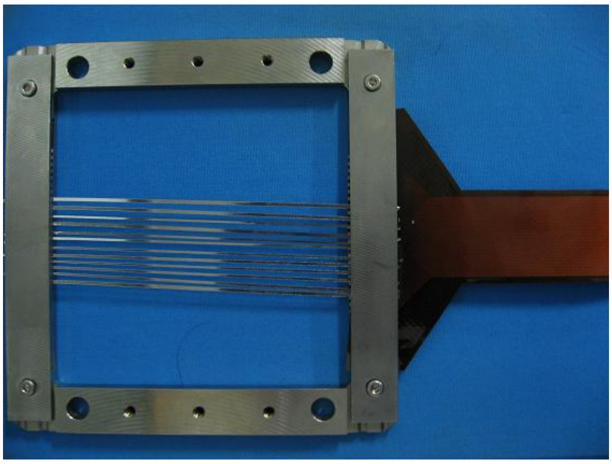

Figure 3.6: Photo of the prototype electrode frame for the arc section.

Chamber

A schematic view is shown in Figure 3.7. The moving guide, which is driven by the stepping motor, is horizontally set in the bulge of the T-tube. The flange of the bulge has two D-SUB feed-throughs made of a metal and a coating glass for the signal readout. The two feed-throughs are separately used for the horizontal and the vertical monitors. As a vacuum seal, we adopt an aluminum knife-edge seal with quick coupling, which enables an easy connection and disconnection, in consideration of the minimization of the radiation work in the beam line. The flange is accurately positioned using knock pins. The relative position between SSEM and the vacuum chamber is measured using a laser tracker beforehand of the installation. The accuracy of the positioning is expected to be ~ 0.1mm.

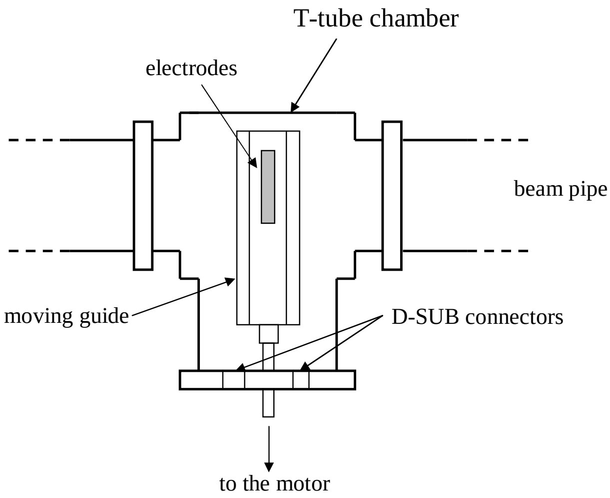

Figure 3.7: Schematic top view of the chamber.

Cables

There are three kinds of cables for SSEM and its surrounding items, the signal cables inside and outside the chamber, and the cable to drive the moving mechanism.

The inside signal cable is used for the connection between the electrodes and the chamber. We use polyimide flexible circuit for good radiation hardness and good flexibility of the cable. A photo of the prototype is shown in Figure 3.8. A D-SUB connector made of PEEK is directly attached to the cable in one end, and SSEM cahode strips are directly attached to the other end.

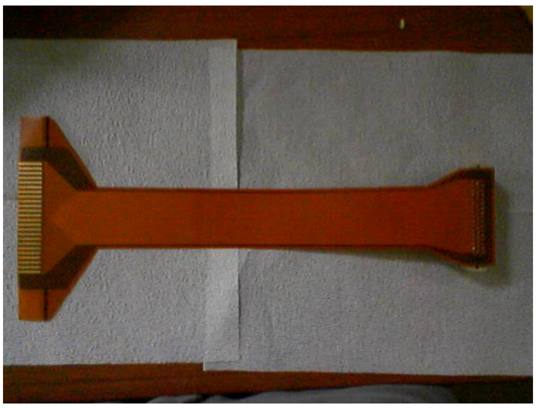

Figure 3.8: Photo of the inside signal cable.

We use two types of the cables for the connection between the chamber and the readout system. This cable consists with the two cables by cascade connection. The cable near the beam line is made of polyimide, which has good radiation hardness, and the farther cable is made of polyethylene specified as non-halogen (NH) cable. The length of the nearer cable is about 3mm and the farther about 100-150mm.

Both the inside and outside signal cables have a pair of two lines per channel of SSEM. In particular, the cable outside the chamber consists of a bundle of twisted pairs. Two adjacent lines of the inside cable and a pair of the outside cable are used for one channel. This structure is expected to suppress noise. The strategy is as follows; one of the two lines, "signal line", is connected to a strip of the cathode and to a positive input of the readout device with differential input (see, Chapter 4). The other one, "noise line", is connected to a negative input of the readout device but not connected to a strip, that is to say, floating. Under this connection, it is assumed that the signal line picks both signal and noise, but the negative line picks only noise. If the noise shape on the two lines is identical, the noise can be removed subtracting the waveform on the noise line from the waveform on the signal line. The effect of this strategy is confirmed by the beam test (described in Chapter 5).

As the motor cable, we use a similar cable to the outside signal one, by connecting the nearer polyimide and the farther polyethylene cables.

Moving mechanism

The moving mechanism mainly consists of a moving guide and a stepping motor.

Figure 3.9 shows a schematic view and a photo of the guide attached to the flange. The whole parts of the moving guide are made of stainless-steel except for the shaft. Using the different material for the shaft is useful to suppress a friction. As the bearing, we plan to use OILES bearing (manufactured by OILES), which is a bearing with carbon graphite powder instead of oil for lubrication because any liquid lubricant becomes solidified under the cryogenic temperature. Two limit switches are bolted to the guide to determine the absolute position of the electrodes.

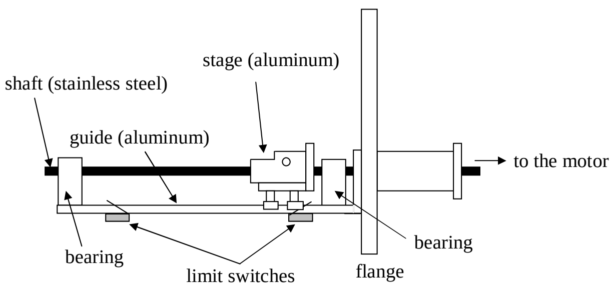

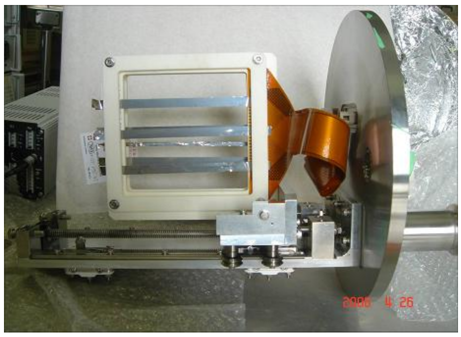

Figure 3.9: Schematic view and a photo of the moving guide attached to the flange.

The check of the positioning accuracy of SSEM is one of the most important issue in the R&D. The positioning accuracy of ~ 0.1mm is required by the beam line simulation as described in Section 2.2. To check the accuracy, we make a test bench and several tests have been carried out. Figure 3.10 shows a photo of the test bench. The moving guide can be seen on the left side and the stepping motor on the right side. So far, we have conducted 20,000 shuttle operations for the accuracy check. A laser tracker is used for the absolute position reference. This examination have shown the position reproducibility of $\sim$ 0.1mm (one sigma). This result satisfies the requirement and indicates that the total positioning accuracy, including the chamber positioning accuracy and the moving mechanism positioning one, is $\sim$ 0.14mm.

Figure 3.10: Photo of the moving mechanism test bench.

3.4 Irradiation test

To check the radiation hardness of the SSEM components, we have carried out irradiation tests using an intense Co^{60} radiation source at JAERI (Japan Atomic Energy Research Institute) Takasaki. The first stage of the test is finished. We are now proceeding to the second stage. In this section, we briefly report the results of the first test.

Figure 3.11 shows a photo of the test scene. A stepping motor, an inside signal cable, a limit switch, and other equipments can be seen. The total radiation dosage for each item is summarized in Table 3.2. The expected radiation dosage in the J-PARC neutrino beam line is estimated to be 0.1-1MGy per year near the beam line. The irradiation dosage in the test, therefore, corresponds to $\sim 3 - 30$ years. After irradiation, all items show their proper performance.

To study the motor performance, a potentiometer, which is a fine variable resistor, is attached to the motor shaft. The resistance of the potentiometer should reflect the rotation accuracy of the motor. Figure 3.12 shows the resistance reproducibility at various test periods. The figure indicates the reproducibility of less than 10Ω, which corresponds to 2μm position accuracy. This accuracy is reasonably small compared to the monitor resolution and other positioning accuracy of $\sim$ 0.1mm.

3.5 Cryogenic test

The J-PARC neutrino beam line equips the superconducting magnets in the arc section. The superconducting magnets require the proper performance of the beam line components under the cryogenic temperature of $\sim$ 80K. Our SSEM must also tolerate the cryogenic temperature.

Figure 3.11: Photo of the irradiation test scene.

Item	Radiation dosage (MGy)
Stepping motor	3.13
Limit switch	2.96
Inside signal cable (polyimide)	4.21
ETFE cable	1-2

Table 3.2: Radiation dosage.

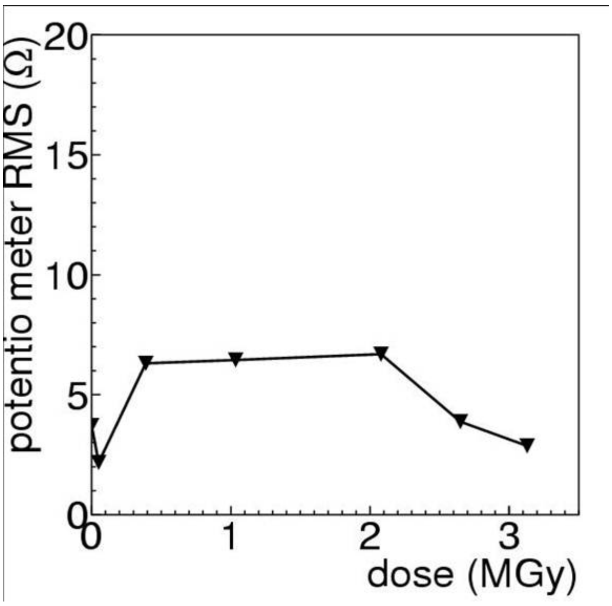

Figure 3.12: Resistance reproducibility of the potentiometer attached to the motor.

To check the SSEM performance under the cryogenic temperature, we carry out a test using liquid nitrogen in KEK. Figure 3.13 shows a photo of the test scene. The moving system is put inside of the vacuum chamber and is kept as vacuum of 3×10^{-2}Pa. The vacuum chamber is cooled down by the liquid nitrogen. The temperature of the moving system is measured using thermo coupling tube to be 89K at the moving test. We confirmed that the moving system work without any mechanical problem at this condition. A torque increase of the shaft is measured to be from 0.2Nm(room temperature) to 0.5Nm (cryo-temperature), which is small enough compared with the motor torque 3Nm.

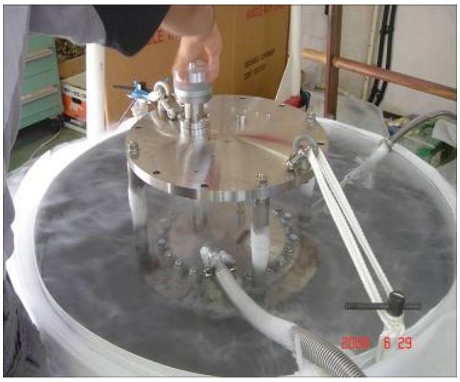

Figure 3.13: Photo of a cryogenic test scene.

Chapter 4

Electronics system for SSEM

In this chapter, we describe the electronics system for SSEM. It consists of three kinds of devices (attenuator module, FADC, and readout module) to be developed in the system. We study attenuator module and FADC. In the following sections, we discuss a brief description of the electronics system and attenuator module and FADC in detail.

4.1 Overview

There are two kinds of beam intensity for the beam tuning of the T2K experiment, full and 1/100 intensities as described in Subsection 2.2.2. SSEM should work both of the intensities. The maximum signal amplitude from SSEM widely varies depending on the beam intensity. The expected maximum signal amplitude is $\sim$ 12 volt at the full intensity operation. And we want to measure the signal waveforms from SSEM every beam bunches in a spill, and we adopt FADC as the waveform sampling device. Schematic view of the electronics system for SSEM shown is in Figure 4.1. This system consists of the following three devices:

- Attenuator module,
- FADC, and
- Readout PC (COPPER module).

These modules acquire channel-by-channel signal waveforms every one beam bunch. Firstly, the signal from SSEM comes into the attenuator module to attenuate the signal amplitude. Then the attenuated signal is digitized by the FADC. Finally, the digitized data is transferred to the readout module to deliver data to the DAQ system for the beam line control. One attenuator, three ADC modules and one readout module are used per monitor.

The attenuator module is a VME 9U module controlled by a VME controller. This module is necessary only for the full intensity beam operation. In the full intensity operation, the signal height becomes one hundred times larger than that in the 1/100 intensity beam. To successfully receive such a large signal, the attenuator module is useful for adjusting the signal level to match the input range of the FADC. We describe the circuit design of this module and the basic performance of a prototype in Section 4.2.

For the FADC, ADC65 (developed by KEK Online-electronics group) is chosen to obtain required SSEM performance. And its basic behavior is well understood in the beam test

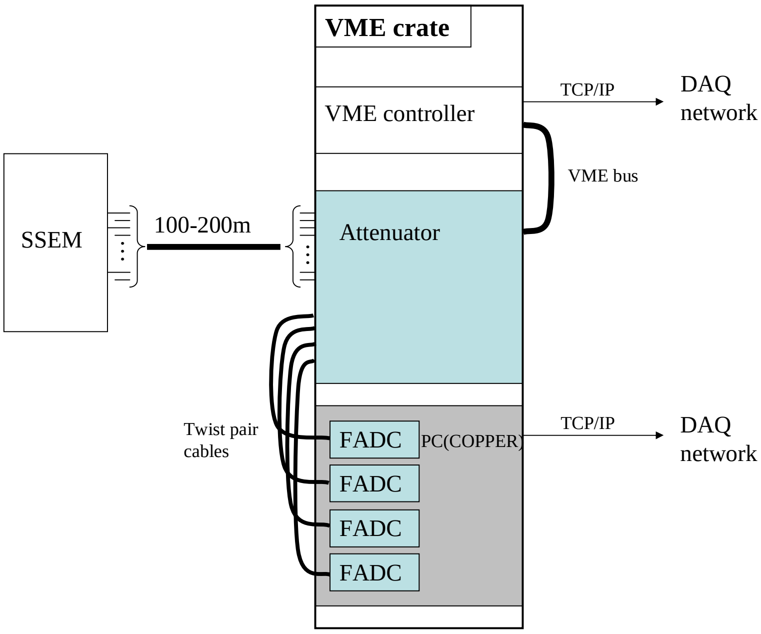

Figure 4.1: Schematic view of the whole readout system for SSEM.

(in Chapter 5). One feature of ADC65 is a capability of the signal shaping for successful A/D conversion. We describe optimization of the time constant of the shaper in Section 4.3.

As a readout module, we employ COPPER (developed by KEK Online-electronics group) which is a VME 9U module with four "finesse" slots. Many kinds of finesse modules (finesse modules) including ADC65 have been developed. COPPER is onboard PC running Linux and makes it possible for us to process data online and transfer them via TCP/IP directly without VME bus. Figure 4.2 shows COPPER module.

4.2 Attenuator module

Here we describe the detail of the attenuator module. The attenuator module is required to have:

- Number of channels per module ≥ 24,
- Differential input type,
- Differential output type,
- Input impedance: 100Ω,
- Output impedance: 100Ω,
- Three attenuation levels of 1/1, 1/8 and 1/64,
- Electrical switches (to control the attenuation level),

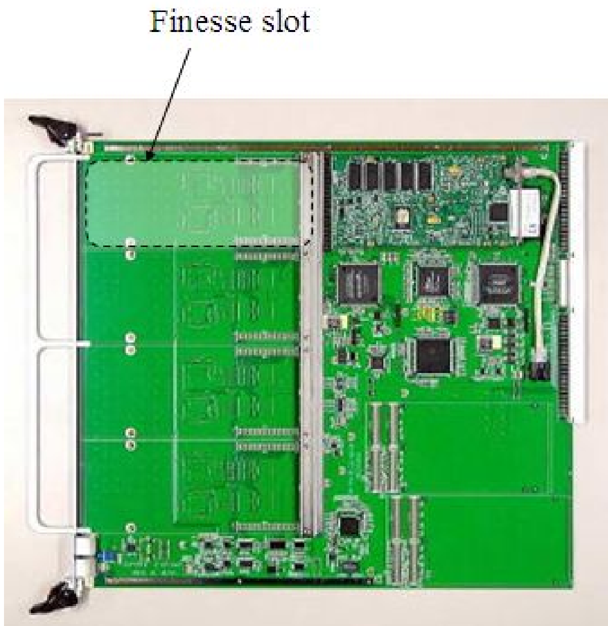

Figure 4.2: Photo of a COPPER module.

- Input dynamic range: to be ±0.2volts(at no attenuation), $\pm \sim 12$volts(at 1/64 level attenuation), and
- Output dynamic range of $\pm \sim 0.2$volts.

These specifications are determined to satisfy the SSEM specifications. For example, the input dynamic range covers the expected signal range of SSEM. The electrical switches are used to synchronize between the beam intensity and the attenuation level automatically. It is not realistic to change the level by hand for all channels because there are too many channels (400) to do. As for the attenuation levels, 1/1 level is expected to receive the signal for the 1/100 intensity operation, 1/64 level for the full intensity operation. 1/8 level is a supplement. In the following subsection, we discuss the design of the attenuator module and its performance.

4.2.1 Circuit design of the analog part

Figure 4.3 shows a schematic view of the circuit design of one channel. In this figure, the positive line is only described. The circuit of the negative line is the same as the position one. At the input stage, there is a T-type attenuation circuit adjusting the total impedance to be 100Ω for impedance matching. For the attenuator level selection, we use the analog switch, ADG409 manufactured by Analog Devices. ADG409 is a CMOS switch with digital control input. This kind of switch has a finite on state resistance. In fact, ADG409 has on state resistance of $\sim 50\Omega$. The on state resistance has a strong dependence on the input voltage, which can deteriorate the linearity. To avoid this problem, we put the buffer amplifier, AD8055 manufactured by Analog Devices, just after the switch for impedance conversion.

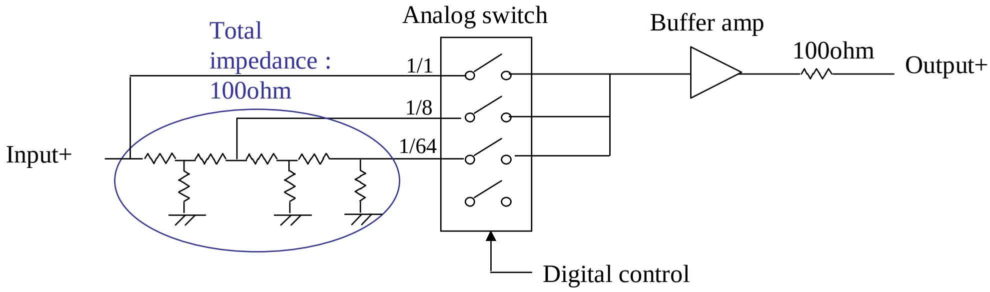

Figure 4.3: Circuit design of the attenuator module.

In addition to the above circuit, we plan to add the test pulse generator on the real board. This generator is used to check the gain of ADC65 that is put downstream.

4.2.2 Performance

To examine the performance of the above circuit, we make a prototype with one signal input and test it. The prototype is shown in Figure 4.4.

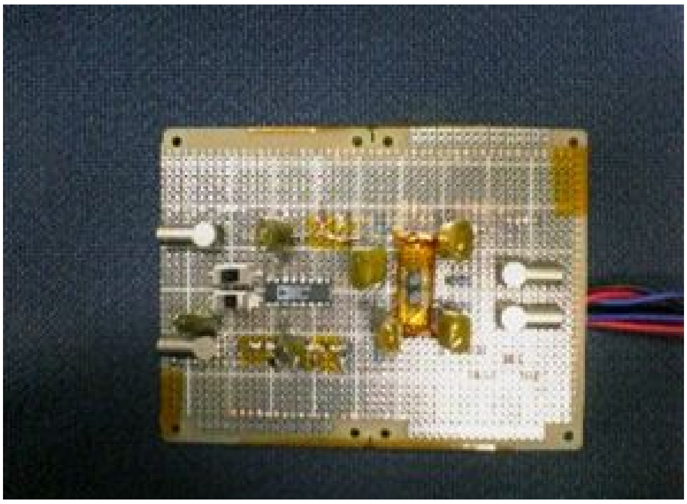

Figure 4.4: Photo of the handmade prototype attenuator

Output waveforms for test pulses are shown in Figure 4.5. The input test pulse is a square pulse with the width of $\sim$ 100nsec and the height of $\sim$ 1volt. The shape of the output waveforms looks good for all attenuation levels. The rising time is sufficiently fast compared to the shaping time of ADC65 described later. There are no ringing and no overshoot.

The linearity of this circuit is also checked. The switch and the buffer are possible to distort the linearity. To investigate the linearity of those parts, we perform the linearity check at the 1/1 level. Figure 4.6 shows the result. We find that the non-linearity is less than 0.25%. According to the beam test and the simulation study described in Chapters 5 and 6, the gain deviation of the whole system is expected to be $\sim$ 2%, the non-linearity of

0.25% is well below the gain deviation and is good enough to keep the monitor resolution.

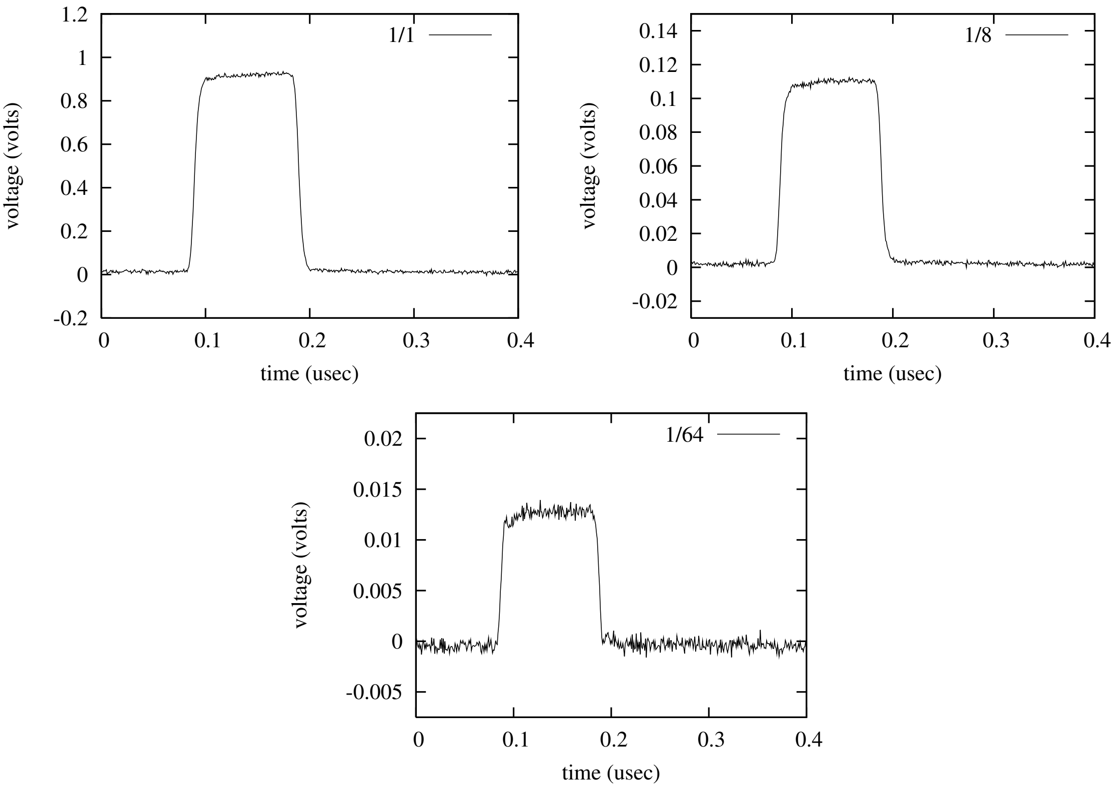

Figure 4.5: Output waveform of the prototype attenuator for each attenuation level.

4.3 FADC

Here we describe the detail of ADC65. Figure 4.7 shows a photo of ADC65. The circuit design of the analog part of ADC65 is shown in Figure 4.8. The important specifications of ADC65 are as follows:

- Number of channels of 8,
- Maximum sampling rate of 65MHz,
- A shaper amplifier per channel,
- Input impedance of 100ohm, and
- Differential input type.

The shaper integrates fast signal for successful A/D conversion. The time constant of the shaper can be tuned by replacing a capacitor and/or a resistor.

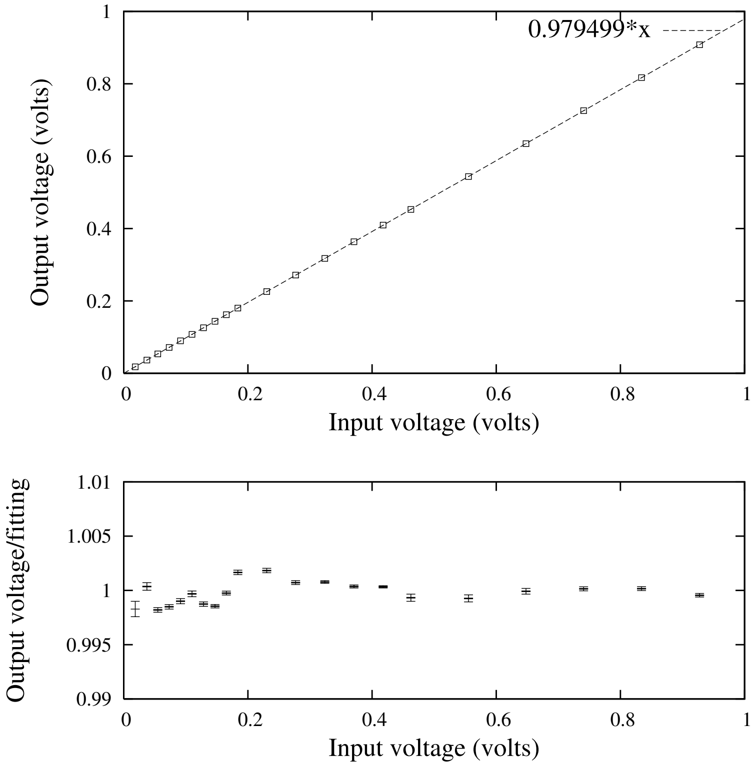

Figure 4.6: Linearity of the prototype attenuator.

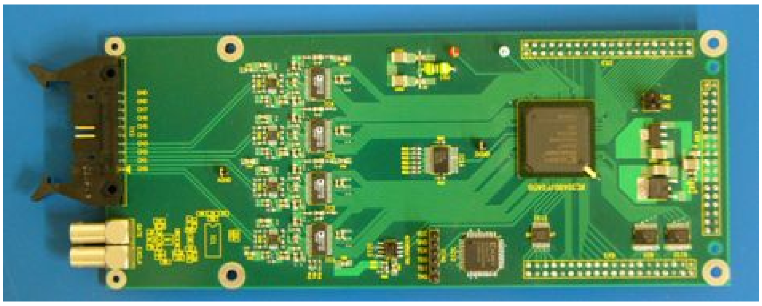

Figure 4.7: Photo of ADC65.

4.3.1 Study of the shaping time

The signal shape in the J-PARC neutrino beam line is expected to consist of eight pulses with the time interval of 600nsec based on the bunch structure of the beam. If we can extract the correct pulse height for each bunch, we can obtain the bunch-by-bunch beam profile, which is useful to understand the beam behavior. We studied the capability of the bunch-by-bunch pulse height extraction by tuning the time constant of the shap.

To study the effect of the time constant, we make four ADC modules with different time constants: 0nsec, 50nsec, 100nsec and 350nsec. We input two kinds of test signal, single-pulse signal and eight-pulses signal. The single-pulse responses of the modules are

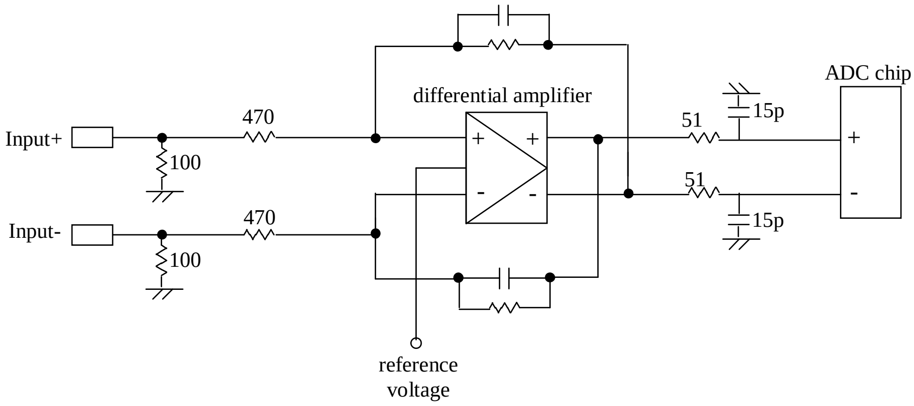

Figure 4.8: Circuit schematic of the analog part of ADC65. One channel part is shown.

used to make a digital filter described later. The eight-pulses signal consists of eight pulses with the time interval of 600nsec reflecting the bunch structure of the beam. The shape of each pulse is determined to resemble a measured waveform in the beam test (see, Figure 5.6). Figure 4.9 shows an input signal taken by a ADC module with no shaper. We find low frequency noise on the baseline. This noise is confirmed to be coming from the signal generator because the noise still remains if we stop the input signal, but the noise disappears if we disconnect the generator from ADC65. The low frequency noise is removed after applying the digital filter, which is described in below.

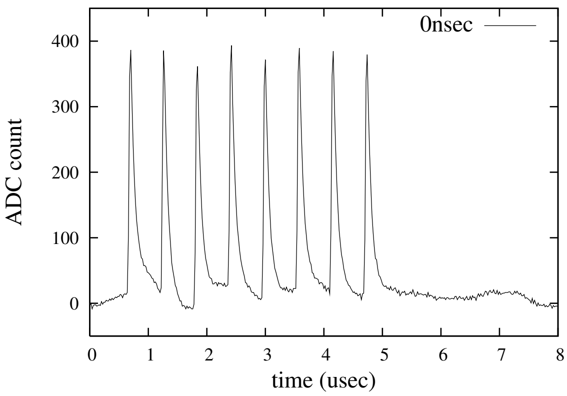

Figure 4.9: Artificial input signal to FADC reflecting the bunch structure at J-PARC.

Figure 4.10 shows responses of the four modules when we input the eight-pulses signal. Pileup can be seen in some plots. To suppress the pileup, we apply a digital filter using Fourier transformation to shorten the pulse length. This filter is set up so that the single-pulse response is transformed into a Gaussian pulse with the time width of 50nsec (one sigma) as shown in Figure 4.11. Using the single-pulse response $S(\omega)$ and Gaussian pulse $G(\omega)$, which are expressed in the Fourier space, the filtering kernel $K(\omega)$ is given by,

$$K(\omega) = G(\omega)/S(\omega). \tag{4.1}$$

Using this kernel, the filtering is expressed by,

$$Y(\omega) = K(\omega)X(\omega), \tag{4.2}$$

where $X(\omega)$ and $Y(\omega)$ are the eight-pulses response and the filtered waveform, respectively. If the eight-pulses response $X(\omega)$ consists of the eight single-pulse responses, the filtered waveform should consist of eight Gaussian pulses. This technique is used by many filtering methods such as deconvolution filters [11]. Figure 4.12 shows obtained waveforms applying this filter to measured eight-pulses waveforms.

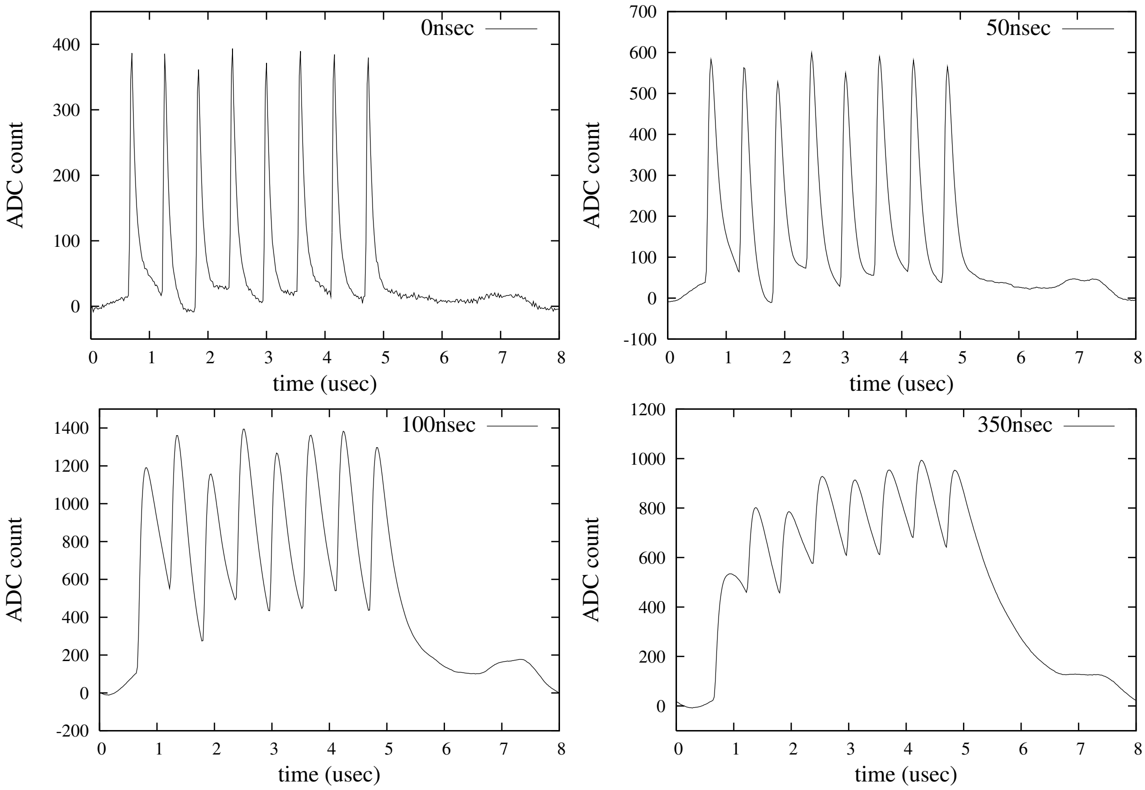

Figure 4.10: Waveform examples measured by four FADCs with different time constants.

After the filtering process, the baseline noise is removed by subtracting a parameterized fitting function of the noise effect from signals. As the fitting function, we adopt a linear coupling of trigonometric functions as given by,

$$f(t, p[]) = \sum_{k=0}^{10} \left(p[2k]\cos(2\pi kt/T) + p[2k+1]\sin(2\pi kt/T) \right), \tag{4.3}$$

where $p[k]$ and T is fitting parameters and the time window, respectively. The result of the baseline subtraction is shown in Figure 4.14.

To evaluate the effect of the difference of the time constant, we extract the pulse height for each pulse from the processed waveforms and calculate the deviation of the pulse heights, which directly affects the monitor resolution. Figure 4.15 shows the deviations vs. the time

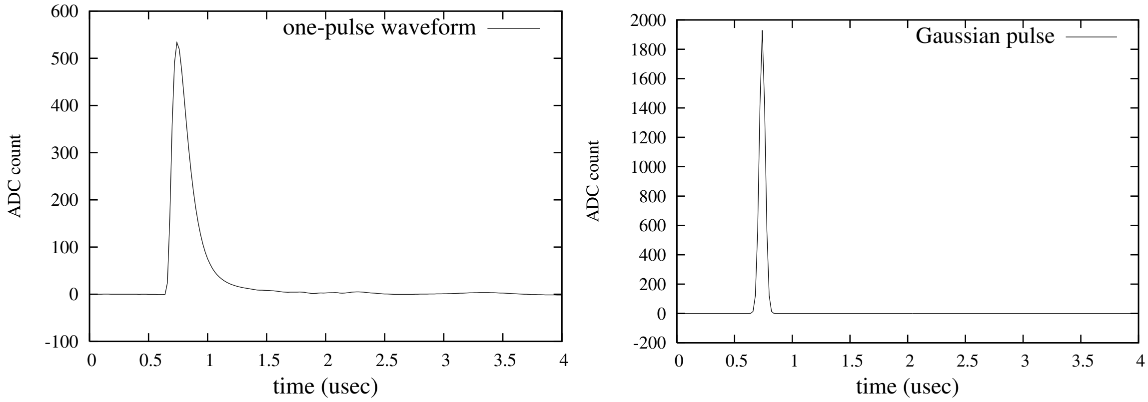

Figure 4.11: Filtering policy that single-pulse waveform (left plot) should be transformed into a Gaussian pulse (right plot). This figure shows the case of the time constant 50nsec.

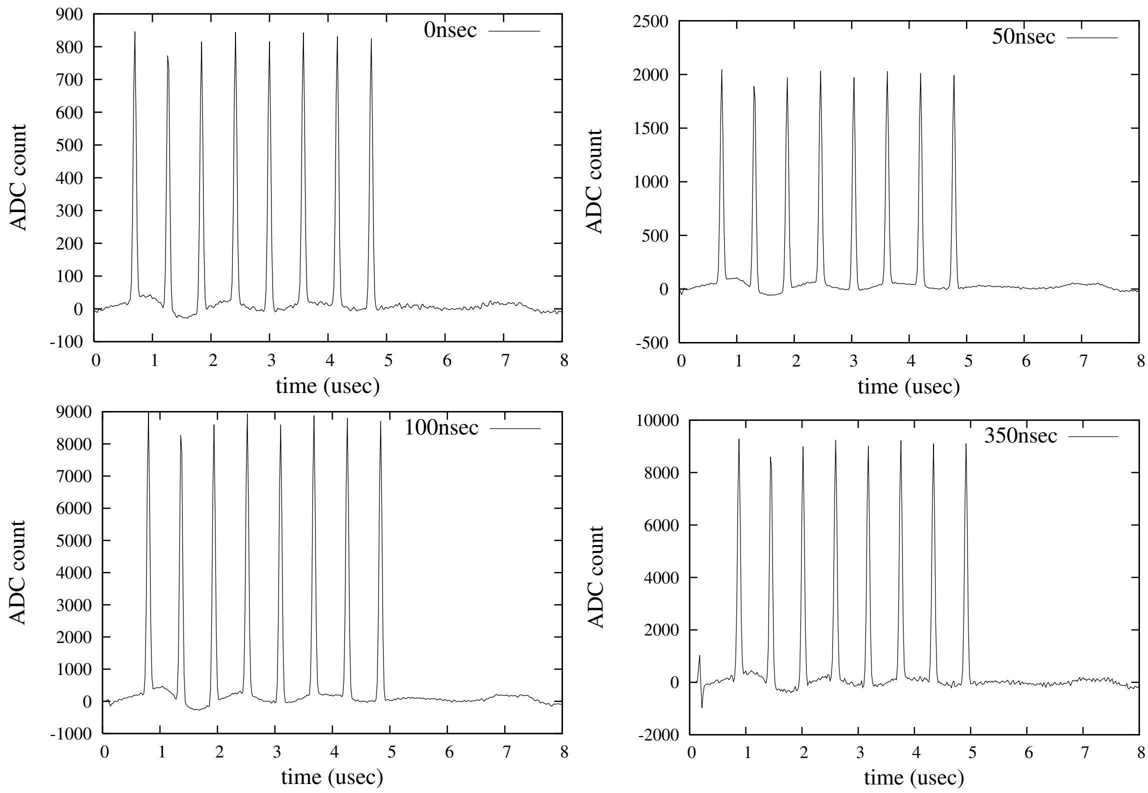

Figure 4.12: Examples of the filtered waveforms.

constants. The figure indicates that the time constant of 50-350nsec is suitable for the J-PARC environment. The zero time constant gives worse performance due to incomplete integration for high frequency components. Assuming no deviation in the input pulses, the degradation of the pulse height precision is turned out to be $\sim 1\%$, which corresponds to the beam position accuracy of 0.03mm and the beam size accuracy of 0.3% for a Gaussian

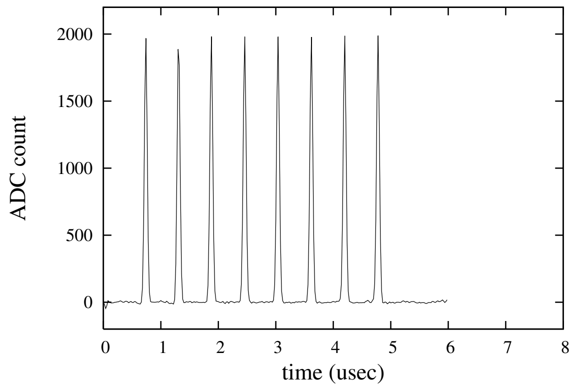

Figure 4.13: Final waveform processed through the filter and the baseline subtraction.

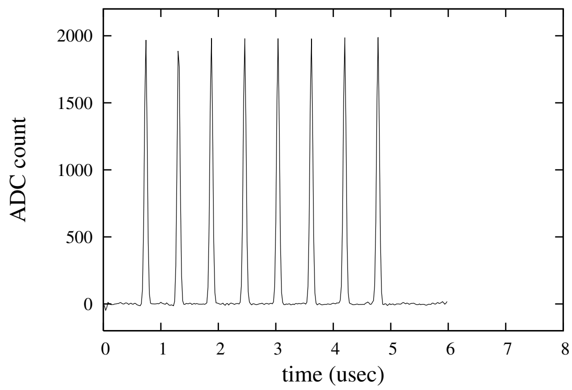

Figure 4.14: Final waveform processed through the filter and the baseline subtraction.

beam with the beam size of 15mm. This is good enough to obtain the bunch-by-bunch profile successfully. Finally, we chose 50nsec as the time constant because 50nsec provides the best performance among this measurement and preserves the original signal shape well.

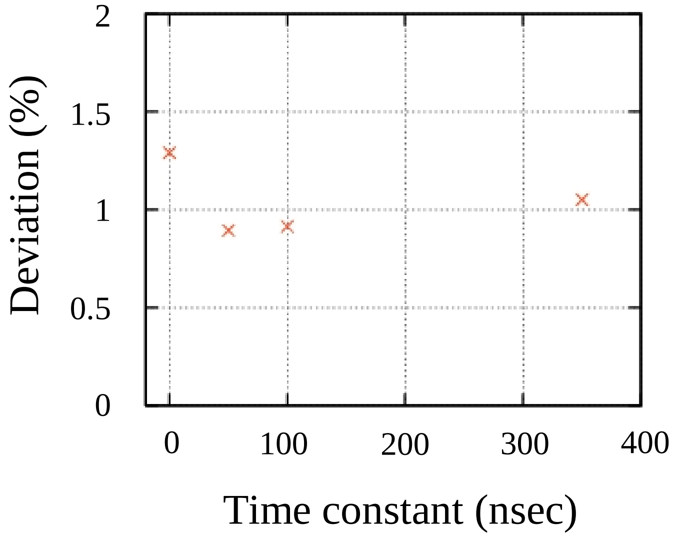

Figure 4.15: Deviation of the measured pulse height vs. time constant of the integration

Chapter 5

Performance study of SSEM using a test beam

In this chapter, we describe a performance study of SSEM using a test beam. The simulation study complements the performance evaluation in the next chapter.

As described in Section 2.2, the requirements for performances of the profile measurement are,

- Beam size measurement resolution of less than 3.5%,
- Beam position measurement resolution of ~ 0.25mm,
- Long term gain stability.

The beam test result enables a rough check of the measurement resolution. The check result also gives the input for the simulation study in Chapter 6.

5.1 Experimental setup

Overview

First, we construct a prototype SSEM and its surrounding components for the beam test. We use the NML beam line, which is an extracted line from the booster ring of KEK-PS at KEK. It supplies a proton beam for neutron and meson experiments. The comparison of the NML beam line and the J-PARC neutrino beam line is shown in Table 5.1.

Figure 5.1 shows a schematic view of the beam test setup. Two identical monitors are arranged closely in the chamber (we call "ssem1" and "ssem2"). Both monitors are set up to measure the horizontal beam profile. The aim of this structure is to evaluate the resolution of the monitor by calculating the difference of the two profiles taken by the two monitors. At J-PARC, in the real case, "ssem1" and "ssem2" will be set up in the different directions (horizontal and vertical) as described in Section 3.3. The design of the electrodes in the beam test is described later.

As readout devices, ADC65 and COPPER (described in Chapter 4) are chosen. The attenuator module is omitted because the signal range in the beam test is acceptable for the input range of ADC65. ADC65 is a 12bits FADC module with shaping amplifiers. It has a maximum sampling rate of 65MHz, a differential input, and an input impedance of

	NML	J-PARC
Beam Energy (GeV)	0.5	50
# of bunches per spill	1	8
# of protons per bunch	2×10^{12}	0.37×10^{12} (for 1/100 intensity)
Repetition rate(Hz)	20	0.25
Beam shape	Gaussian	unknown
Beam size (mm)	3.6 (1σ of Gaussian)	6-33

Table 5.1: Comparison of the NML beam line and the J-PARC neutrino beam line. The beam size of the NML beam line is the size at the installed position of our monitor.

50ohm. This time constant of the shaper is set to 1μsec, which is long enough for successful A/D conversion. This time constant is different from the current design because we didn't know the signal shape at that time.

As for the moving mechanism and other mechanical structures, they were not implemented in this test. The monitor is, therefore, always exposed to the proton beam.

Cables

For the connection between the electrodes and the chamber, a prototype cable with print pattern sandwiched by polyimide films is used (see, Section 3.3). For the connection between the chamber and ADC65, $\sim$ 150m ETFE twist pair cables are used. The connection of the signal cables is described in Section 3.3. The cables have two lines per strip. One of the two lines (signal line) is connected to a strip of the SSEM and a positive input of the FADC, and the other one (noise line) is connected to a negative input of the FADC but not connected to the SSEM, that is to say, floating. The purpose of this structure is to reduce noise picked in the signal transmission.

Design of the electrodes

A schematic view of the electrodes is shown in Figure 5.1. A photo of the electrodes attached to the flange is shown in Figure 5.2. There are two cathodes and three anodes. The two identical SSEMs, "ssem1" and "ssem2", share the center anode. In the current design, however, the side anodes have been removed as described in Section 3.3 because the necessity of the side anodes is confirmed just in this beam test.

The electrodes are all made of titanium foils with the thickness of 5 μm as in the case of the current design, and ceramic frames, which is different from the current design. Ceramic is the optimal material in view of its radiation hardness, thermal conductivity and insulation property. The choice of the stainless-steel frame in the current design is based on a cost issue.

The segmentation design of the cathode electrode is shown in Figure 5.3 and a photo in Figure 5.4. The cathode consists of 24 strips with different widths and uniform spacing (1mm). This design is expected to cover a wide range keeping the fine segmentation near the center of the monitor.

As for the anodes, applied high voltages are basically $\sim$ 100volts, which is large enough for signal gain to saturate. The voltages can be applied to the center anode independently

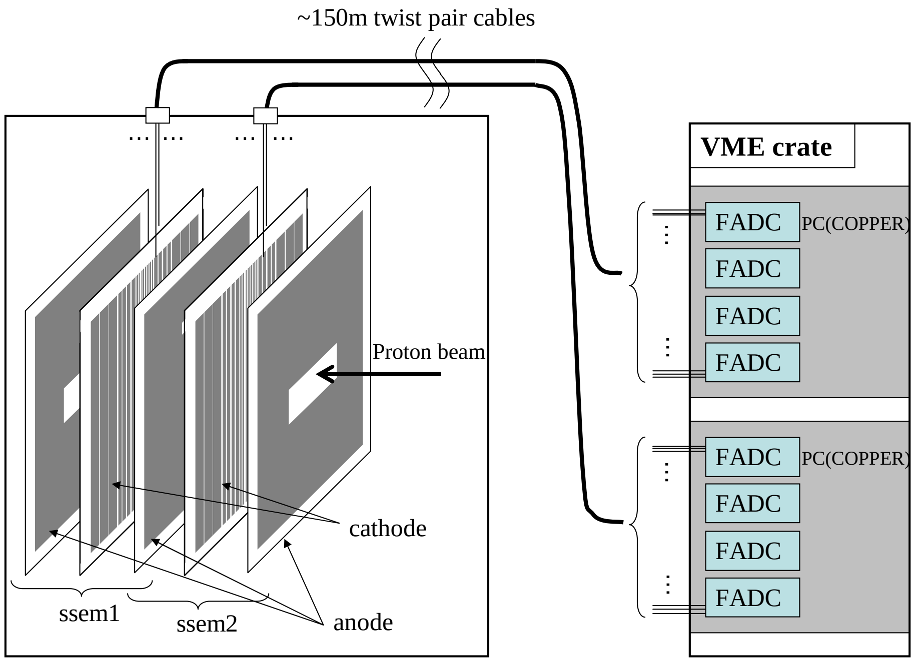

Figure 5.1: Schematic view of the beam test setup.

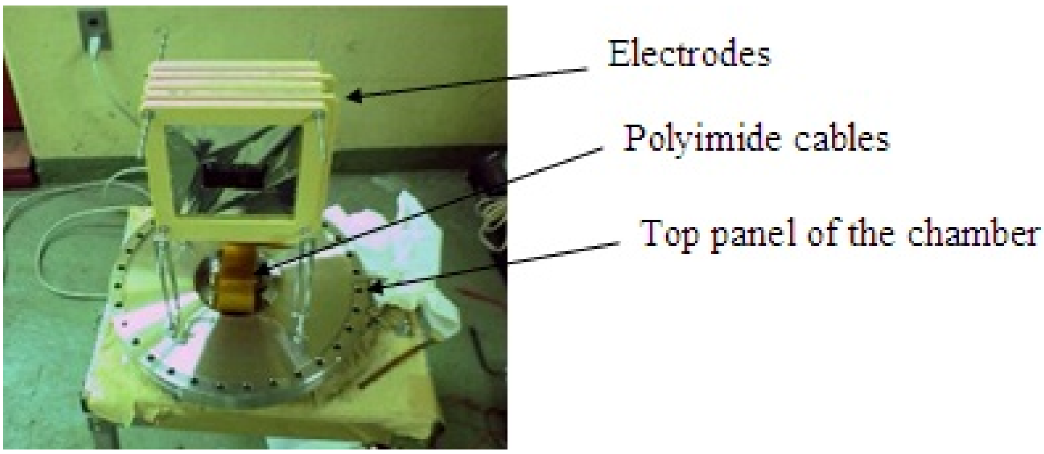

Figure 5.2: Photo of the core part of the prototype SSEM.

of the side two anodes. This advantage is useful to check the effect of the side anodes. The side anode foil has a rectangle hole in order for the beam not to hit. This structure is expected to avoid the beam loss. Figure 5.5 shows a photo of the side anode.

5.2 Results

The results of the beam test are described below.

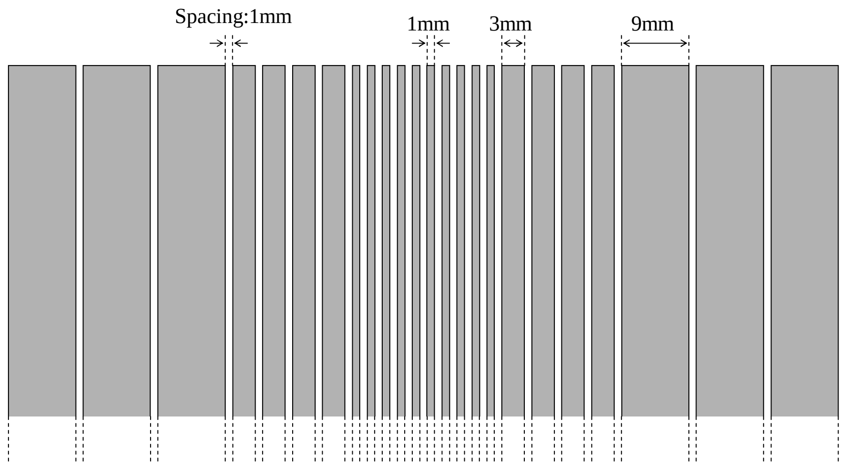

Figure 5.3: Segmentation design of the cahode.

Figure 5.4: Photo of the cathode.

Figure 5.5: Photo of the anode.

Output waveforms

Figure 5.6 shows a measured signal on one channel of the prototype SSEM taken by a differential oscilloscope TPS2024 (manufactured by Tektronix). Figure 5.7 shows a measured signal taken by ADC65, the sampling rate of which is set to 50MHz. These signals synchronize with the beam timing trigger. The waveform taken by ADC65 has offset of 1300 ADC count. The offset is in the range of 1000-2000 for every channel.

Effectiveness of the noise subtraction

Figure 5.8 shows the effect of the noise subtraction method using the twist pair cable. Two waveforms on the left side show original signals on the signal and noise line of the twist pair. The waveform after the noise subtraction (signal line - noise line) is shown on the right side. According to this figure, our noise subtraction method is working effectively.

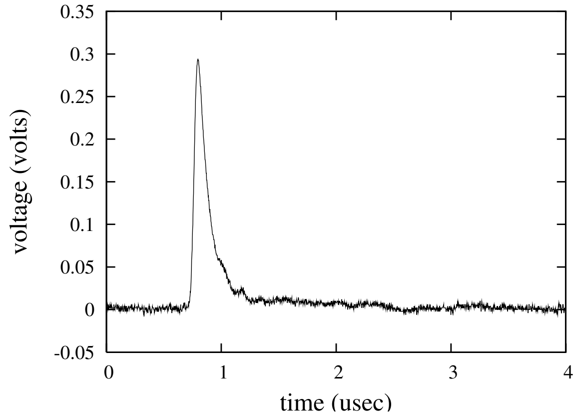

Figure 5.6: Measured signal taken by the differential oscilloscope TPS2024.

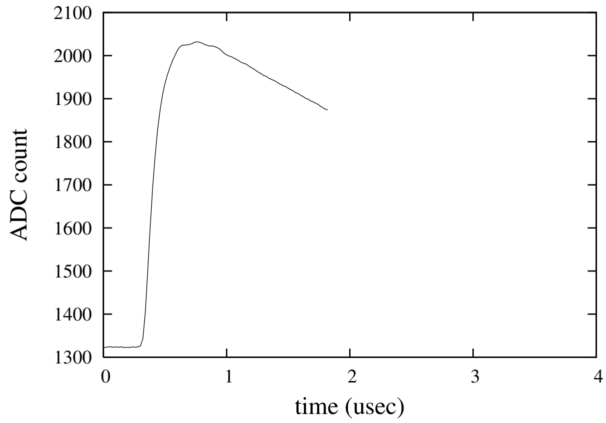

Figure 5.7: Measured signal taken by ADC65 with 1μsec shapers.

Profile reconstruction

Examples of the reconstructed profile are shown as solid histograms in Figure 5.9. The dotted lines show fitted Gaussian curves. The profile reconstruction process is as follows,

1. remove the offset from the signal waveform taken by ADC65,

2. extract the signal height on each channel, and

3. plot the signal heights normalized by the strip widths for the strip center positions,

where the signal height is defined as average of the signal at a certain time window. We have confirmed that the influence of the window selection can be ignored.

Verification of the obtained profile

To verify the correct behavior of our monitor, we examine the beam position dependency of the profile. Figure 5.10 show the measured profiles when the beam position is moved to

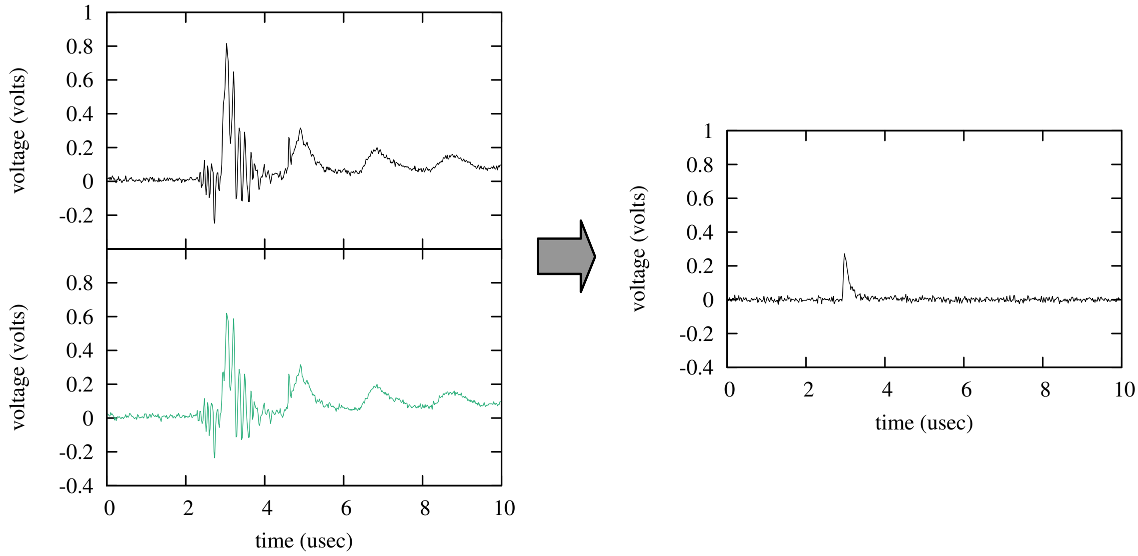

Figure 5.8: Effect of the noise subtraction method. The upper plot on the left side shows a measured signal on the signal line. The lower plot shows one on the noise line. The right plot shows the difference of them (signal line - noise line).

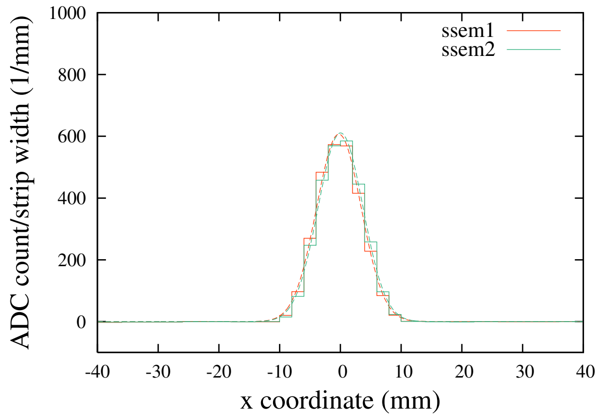

Figure 5.9: Reconstructed profile using the measured waveforms by ADC65. The red and the green correspond to “ssem1” and “ssem2”, respectively.

left and right side, respectively. The response of the monitor is reasonable. In addition, the extracted beam size from the profile is about 3.6mm (1σ of Gaussian) independent of the beam position. The more precise study for the beam size is described later.

To believe the correctness of our monitor more firmly, it is useful to compare our monitor with another monitor originally equipped in the NML beam line. Figure 5.11 shows a profile measured by another monitor, which is made of tungsten wires arranged with 2.5mm pitch, and the extracted beam size from its profile is 4.6mm as 1σ of Gaussian. Comparing our monitor's results with these ones, the shape of the profile is consistent and looks like Gaussian in both cases but the beam size is different. This difference can be understood by the difference of the installation locations.

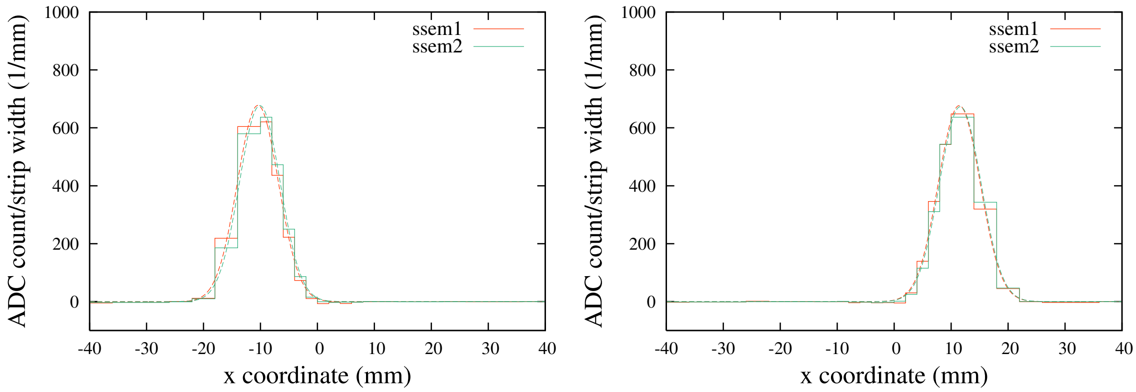

Figure 5.10: Measured profiles when the beam position is moved to left and right side.

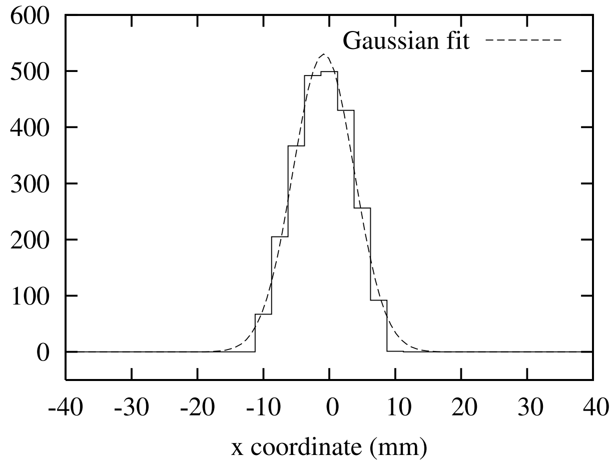

Figure 5.11: Profile example measured by another profile monitor used in the NML beamline.

Correlation between the beam intensity and the profile area

If the measured profile is proportional to the beam intensity, we can more firmly believe that the measured profile correctly reflects the beam profile. The correlation check between the beam intensity and the profile is useful for it.

As an indecator correponding to the beam intensity, we adopt the profile area which is expressed as A in the following equation,

$$\frac{A}{\sqrt{2\pi}\sigma}\exp\left(-\frac{(x-x_c)^2}{2\sigma^2}\right). \tag{5.1}$$

The profile area A is a better indecator than the profile amplitude or height because the beam size slightly varies if the beam intensity changes.

Figure 5.12 shows measured profiles in four different beam intensities: 2.15×10^{12}ppp, 1.10×10^{12}ppp, 0.54×10^{12}ppp and 0.32×10^{12}ppp. The different colors correspond to the different intensities. According to the figure, the response of our monitor looks reasonable. The profile area has been extracted fitting those profiles, which are plotted in Figure 5.13. Good linearity can be seen in the figure. By this study, it is also confirmed that the beam intensity "per bunch" for the 1/100 intensity beam at J-PARC, 0.37×10^{12}, is in the linear range.

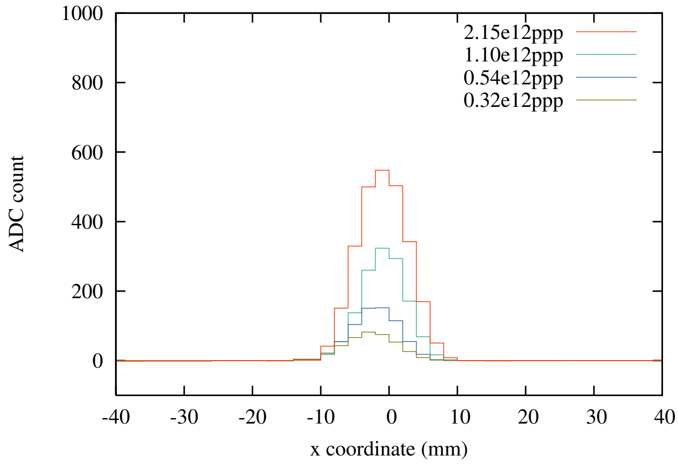

Figure 5.12: Measured profiles in various beam intensities.

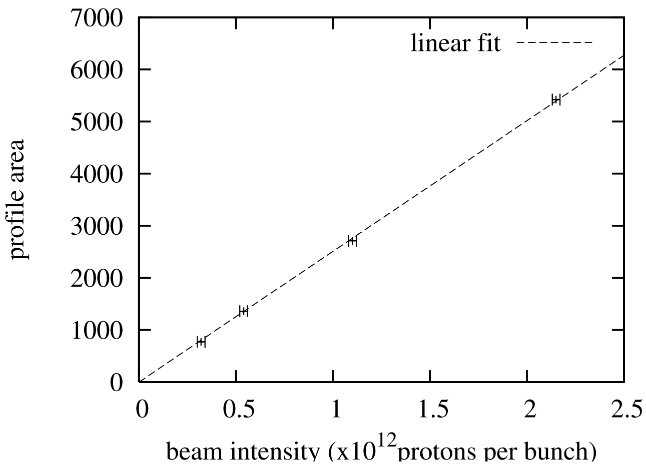

Figure 5.13: Correlation between the beam intensity and the profile area.

Dependence of gain on the anode voltage

As described above, three anodes are laid in the prototype SSEM to collect secondary electrons, and the center anode and the side two anodes can be applied high voltage independently. We take advantage of it to search for the optimal high voltage setup to obtain the maximum efficiency with minimal exertion.

First, we examine the effect of the side anodes comparing the profile areas for different side anode voltages: ~ -100volts, 0volts and ~ 100volts. In the measurement, the voltage of the center anode is fixed at 0volts or ~ 100volts. Figure 5.14 shows the measured profile areas under these voltage setups. We find no significant dependence of the gain on the anode voltage for the center anode voltage of 100volts, whereas we find the significant dependence for the center anode voltage of 0volts. We don't understand the cause of these dependencies. The further detailed study related to the electric field may be necessary to understand them. Anyway, we conclude that the side anodes can be omitted because the gain does not depend on the side anode voltage if the center anode voltage is applied to be sufficient.

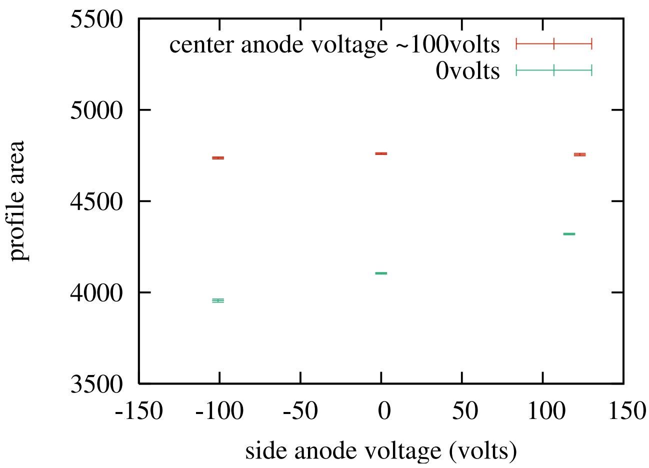

Figure 5.14: Profile area vs. voltage of the side anodes. The red points are the measured data at the center anode voltage of ~ 100volts, and the green points at the center anode voltage of 0volts.

Next, we investigate the effect of the center anode voltage. In almost all measurements in the beam test, ~ 100volts is applied to the center anode because 100volts is large enough for gain to saturate. To confirm the saturation, we check the dependence of the signal gain on the center anode voltage. Figure 5.15 shows signal heights on a certain channel (near the beam center) for various center anode voltages. In the figure, saturation can be seen near ~ 60volts. Thus, we adopt 100volts, which is much larger than that.

Secondary emission efficiency

The secondary emission efficiency is defined as the ratio of the number of secondary electrons to the number of incident protons. Several preceding experiments have reported to be the efficiency of several percent. Here we check consistency of our monitor.

Assuming that the monitor works as a current source, the charge amount on each channel can be estimated by the integral of the measured waveform. In particular, the waveforms taken by the oscilloscope are suitable because the waveform taken by ADC65 is not completely sampled in the gate window. For the conversion between the voltage and

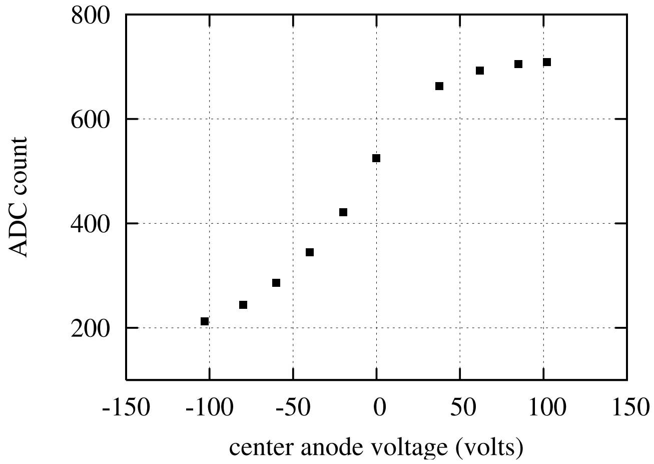

Figure 5.15: Dependence of signal gain on the center anode voltage.

the current, the matching impedance 50ohm is used based on Ohm's law, and after the charge extraction, normalizing the charge amount by the electron charge, the secondary emission efficiency can be obtained.

Figure 5.16 shows the number of secondary electrons for the various beam intensities. The applied high voltage is fixed at $\sim$ 100volts for the center anode and 0volts for the side anodes during the measurement, and the beam intensity is measured by a CT monitor near our monitor. This measurement is carried out after the irradiation of $\sim 1 \times 10^{20}$ protons. The secondary emission efficiency estimated from the figure using a linear fit is 3.3%. This result is consistent with the preceding experiments.

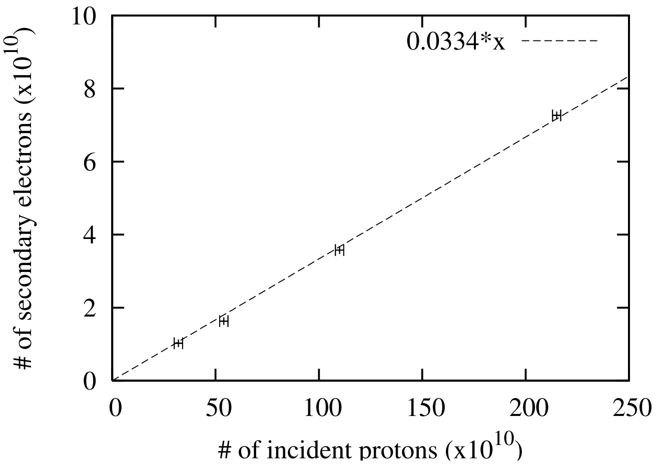

Figure 5.16: Secondary emission efficiency.

Stability of the secondary emission efficiency

Several preceding experiments using SSEM have reported the long term variation of the secondary emission efficiency [14, 18, 19]. This phenomenon is thought to be caused by the reduction of oxide layer or contamination by carbon compound (like CO gas absorption) on the surface of electrodes.

In the J-PARC neutrino beam line, SSEMs are exposed to the proton beam during the beam tuning operations. The secondary emission efficiency must be stable in those operations.

To check the long term gain stability, we compare the profile areas, which are proportional to the secondary emission efficiency, at different test periods (about 3 months). Figure 5.17 shows the profile areas for the beam position at three test perioeds. The integrated number of irradiated protons from the installation is 1.71×10^{19}, 3.87×10^{19} and 9.22×10^{19} at the first, second and third period, respectively. The number of irradiated protons of 10^{19}-10^{20} corresponds to the irradiated proton density of about 10^{19}-10^{20}protons/cm^2 considering the beam size. We find the significant variations of the gain in the figure. About 10% decrease of the efficiency is confirmed at the center of the monitor. On the left side of the monitor, the efficiency rises between the first and the second test period and drops between the second and the third period. The dependence of the variations on the beam position is thought to come from the long term variations of the beam position. The beam position moves by magnet tunings and so on.

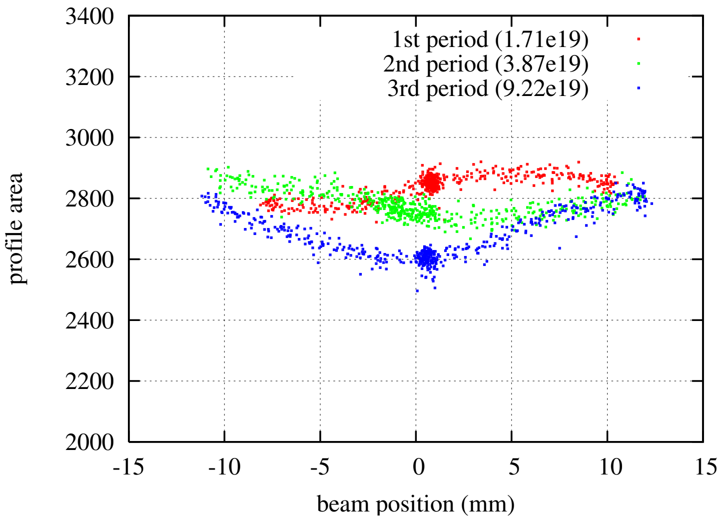

Figure 5.17: Evolution of the profile areas.

The efficiency variation is related to the deterioration of the metal surface. Figure 5.18 shows a photo of the irradiated anode foil used in the beam test. We find the discoloration of the surface near the irradiated point. We don't understand the cause of this discoloration. Heating, reduction of oxide layer and reaction with the residual gas are possible.

In the CERN SPS beam line, the stability of the secondary emission efficiency was studied for aluminum and titanimum [19]. The integrated number of irradiated protons are close to 1×10^{20}protons/cm^2 (over two years). Figure 5.19 shows the efficiency variation for alu-

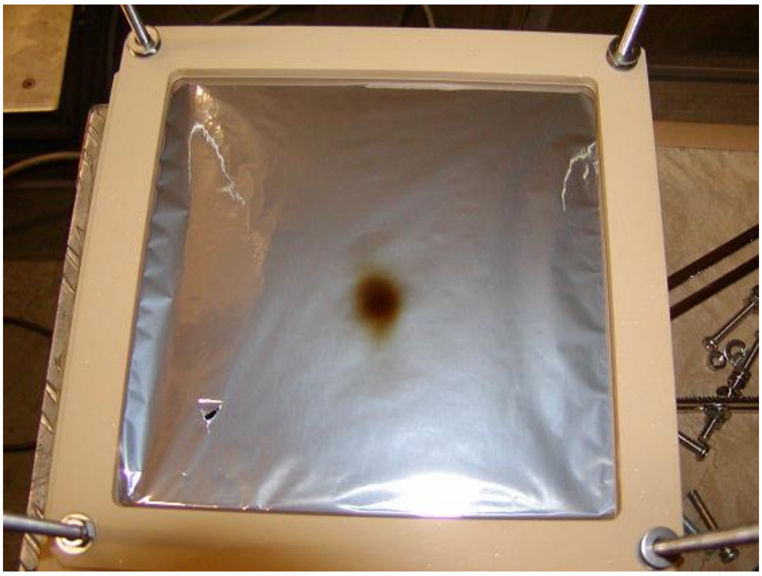

Figure 5.18: Irradiated titanium foil.

minum and titanium foils. The efficiency of titanium is stable up to 1.0×10^{18}protons/cm^2 and slowly rises by 15% before dropping back towards its original value between 10^{18} and 10^{20}protons/cm^2. Our result is consistent with this result. In both cases, $\sim$ 10% variation of the efficiency is confirmed, and the rise and drop of the efficiency for the irradiation of 10^{19}-10^{20}protons/cm^2 are also confirmed.

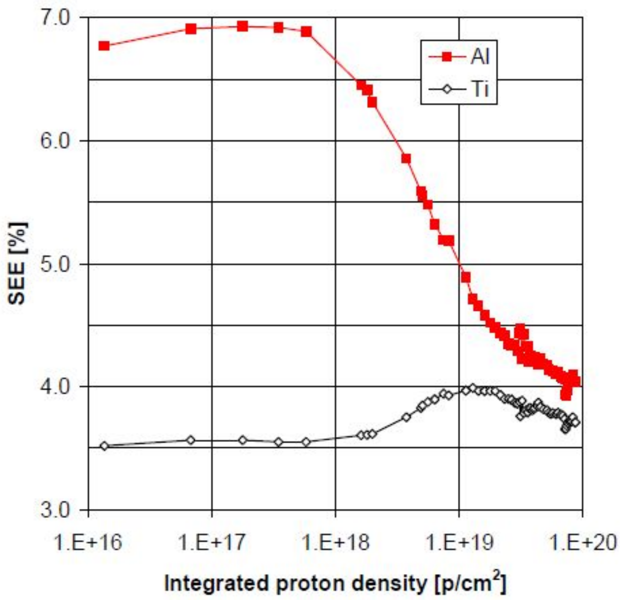

Figure 5.19: Change in the secondary emission efficiency of aluminium and titanium foils in the CERN SPS beam line [19].

If we believe the CERN SPS result, the efficiency is stable up to 1.0×10^{18}protons/cm^2 of irradiation, which corresponds to at least 6×10^5 pulses (spills) or 700hours of exposure time for 1/100 intensity beam at J-PARC. This is thought to be sufficient for the beam tuning. In addition, to correct the efficiency variation, we plan to measure the efficiency periodically at J-PARC.

Profile measurement resolution of the prototype SSEM

The profile measurement resolution is a very important factor of the monitor performance because the resolution directly affects the beam tuning accuracy. Here we evaluate the resolution using the beam test results and compare it with the requirement.

For the resolution evaluation, two identical monitors, "ssem1" and "ssem2", are useful because the difference of the two monitors should include information of the resolution information. We compare the beam positions obtained by the two monitors as follows. First, we extract the beam position and the beam size from each profile by a Gaussian fit. Next, we plot the difference of the fitting parameters between "ssem1" and "ssem2" for various beam positions, and check the deviation of the difference. The deviation should reflect the resolution. In fact, the deviation has been well reproduced by a monitor simulation (described in Chapter 6). Here we temporarily assume the deviation as the resolution though more proper definition and estimation of the resolution are done using the simulation in the next chapter.

The comparison of the beam positions is shown in Figure 5.20. A good correlation between "ssem1" and "ssem2" can be seen in the left plot. The difference between "ssem1" and "ssem2" is shown in the right plot, and there can be seen the offset and the deviation of less than $\sim$ 0.1mm. Assuming the offset is caused by the difference of the structural alignment of the two monitors, we ignore the offset in the resolution evaluation. Under the above assumption and in consideration of the error propagation, the resolution is estimated to be $0.1/\sqrt{2} = 0.07$mm, which is good enough compared with the requirement of 0.25mm.

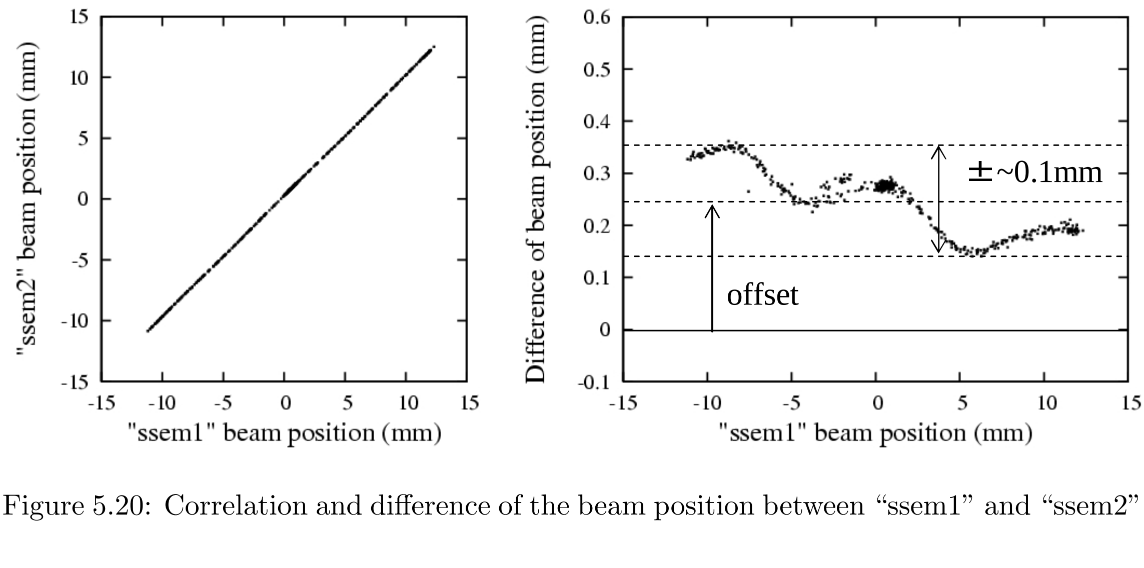

Figure 5.20: Correlation and difference of the beam position between "ssem1" and "ssem2".

We then evaluate the resolution of the beam size measurement. We define 1.68σ of fitted Gaussian as the beam size for consistency with the discussion in Chapter 6. The reason of this definition is also described there. The evaluation way of the beam size resolution is almost the same as in the case of the beam position except for the treatment of offset. We don't ignore the offset in the case of the beam size because the two monitors are set closely enough for the beam size not to change. Figure 5.21 shows corresponding plots related to the beam size, and there can be seen the beam size of $\sim$ 6mm independent of the beam position in the left plot and the deviation of less than 0.15mm in the right plot. By the calculation of the error propagation in the same way as in the evaluation of the position resolution, the resolution is estimated to be 1.8%, which is good enough compared with the requirement 3.5%.

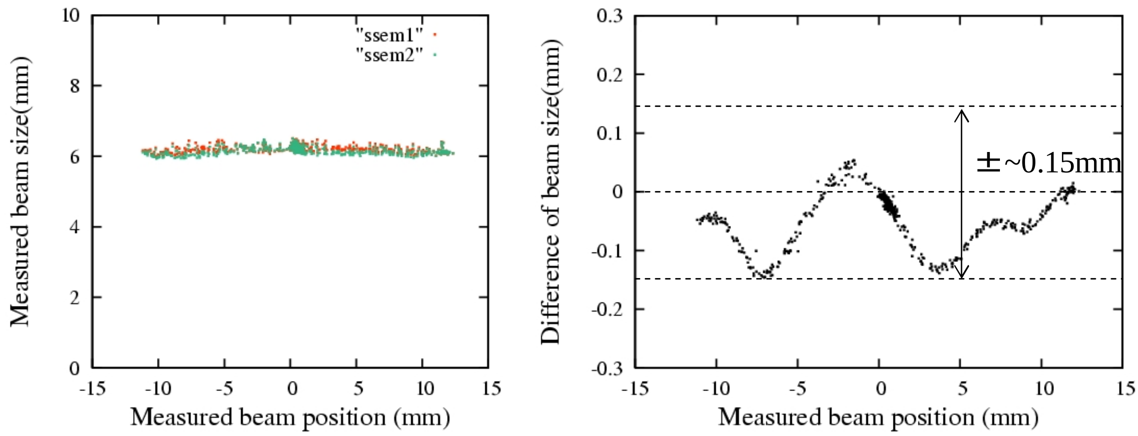

Figure 5.21: Measured beam size and the difference of the beam size between "ssem1" and "ssem2".

5.3 Summary of the beam test

To investigate the basic performance of SSEM and confirm the requirements, we construct the prototype SSEM and carry out the beam test. The prototype contains two identical monitors, which are expected to be useful for the resolution evaluation. As the material of the monitor electrodes, 5μm titanium foils, which will be used for the J-PARC neutrino beam line, are chosen. As readout devices, ADC65 and COPPER are used as designed for J-PARC SSEM, but the attenuator module is omitted.

In the test, channel-by-channel signal synchronized with the beam timing trigger is successfully detected by ADC65 and COPPER. We have also made sure that the noise subtraction method using the twist pair cables works effectively. The beam profiles are reconstructed and the shape of them is verified to be consistent with another profile monitor made of tungsten wires. A correlation between the profile area and the beam intensity is also confirmed and it supports that the measured profile correctly reflects the beam profile.

To search for the optimal high voltage setup and guarantee the unnecessity of the side anodes, some investigations on the gain or the secondary emission efficiency were conducted under different high voltage configurations. By the investigations, $\sim$ 100volts center anode voltage has been turned out to be large enough for gain to saturate and the secondary emission efficiency has been estimated to be about 3.3% after the irradiation of 1×10^{20} protons. The efficiency variation of about 10% is confirmed at the center of the monitor after the irradiation of 1×10^{20} protons. On the left side of the monitor, the rise and drop of the efficiency is confirmed. This result is consistent with the preceding experiment in the CERN SPS beam line [19]. According to the CEAN SPS result, the efficiency of titanium is stable up ot 10^{18}protons/cm^2 of irradiation, which corresponds to at least 6×10^5 pulses (spills) or 700hours of exposure time for 1/100 intensity beam at J-PARC. This is thought to be sufficient for the beam tuning.

Finally, comparing the two identical monitors "ssem1" and "ssem2", the profile measurement resolution of the prototype SSEM is estimated to be,

- Beam size resolution of 1.8%,
- Beam position resolution of 0.07mm.

This result satisfies the requirements, 3.5% in the size resolution and 0.25mm in the position resolution. For more precise study of the measurement performance, we conduct a monitor simulation in the next chapter. The simulation complements the beam test results and also has a capability of the resolution estimation for various conditions including one of the J-PARC neutrino beam line.

Chapter 6

Simulation study of SSEM

The beam test results are very important to understand the basic performance of SSEM. Here we take over the results and proceed to more proper and advanced studies using simulations.

The requirements to be confirmed in this chapter are,

- Beam size resolution of less than 3.5%; and
- Beam position resolution of $\sim$ 0.25mm.

Though rough resolution estimation is done based on the beam test results, described in the previous chapter, we carry out simulations for more precise estimation of the resolutions. The SSEM performance in the J-PARC environment is also estimated.

6.1 Simulation set up

In this section, we describe the set up of the simulation.

Outline of the simulation

The outline of the simulation is as follows. First, we fix the cathode segmentation design and the incident beam profile, and we make imaginary monitors with some error sources described later. Secondly, the imaginary beam is injected into those monitors and the signal height on every channel of the monitor is calculated by the integral of the beam intensity on each cathode strip. Thirdly, the beam profiles are naturally reconstructed by those extracted signal heights. If the cathode segmentation is infinitely fine and there is no error source, the reconstructed profiles should completely correspond to the incident beam profile. Conversely, the reconstructed profiles are distorted by the finite cathode segmentation and the error sources. Fourthly, assuming the distortion determines the monitor resolution, we evaluate the resolution comparing the reconstructed profiles with the incident beam profile by fitting. As the fitting function, the same function as one of the incident beam is used.

Error sources

We assume three error sources, which affect the monitor resolution,

- alignment error of the cathode strips (AE),

- gain deviation of the system (GD), and
- statistical fluctuation (SF).

The alignment error is not the alignment error of the whole monitor but the error of each strip. The gain deviation is the deviation of the channel-by-channel gain determined by the secondary emission efficiency, the gain of readout devices, and so on. The statistical fluctuation is thought to mainly consist of electrical noise. By definition, AE and GD are completely systematic errors, and SF includes both systematic and statistical errors.

The reconstructed profile P_i are expressed using the error sources, AE(δ_i), GD(G_i) and SF(B_i), as follows,

$$P_i \propto G_i \int_{x_i - w_i/2+\delta_i}^{x_i + w_i/2+\delta_i} I(x)\mathrm{d}x + B_i, \tag{6.1}$$

where i, x_i, w_i and $I(x)$ are the strip index, the strip center position, the strip width, and the incident beam profile, respectively.

Beam shape and beam size

Ignorance on the beam shape in the J-PARC neutrino beam line is awkward. In the beam test, the Gaussian profile is detected. The equation is given by,

$$G(x; I, x_c, \sigma) = \frac{I}{\sqrt{2\pi}\sigma} \exp\left(-\frac{(x-x_c)^2}{2\sigma^2}\right). \tag{6.2}$$

On the other hand, several beam line simulations (for example, [12]) uses another beam shape. They assume that the beam particles are distributed flatly in the phase space. That particle distribution makes the following beam shape:

$$S(x; I, x_c, \tau) = \frac{I}{\pi\tau}\sqrt{1-\left(\frac{x-x_c}{2\tau}\right)^2}, \tag{6.3}$$

where x_c, 2τ and I correspond to the beam position, size and intensity respectively. Hereafter we refer to this function as "Sqrt" for convenience. The Sqrt function is thought to be a reasonable beam shape at the start point of the beam line, because particles in the newborn proton beam distribute flatly in the phase space. In practice, however, the beam shape crumbles and becomes like Gaussian during the delivery. Thus, it is valid to assume a middle shape between Gaussian and Sqrt as the expected beam shape.

To obtain the middle shape, we employ a convolution. The equation of the convolution is given by,

$$F(x; \lambda; I, x_c, s) = I\int_{-\lambda s/\rho}^{\lambda s/\rho} S\left(x'; 1, 0, \frac{\lambda}{\rho}s\right) G\left(x - x_c - x'; 1, 0, \frac{1-\lambda}{\rho}s\right) \mathrm{d}x' \tag{6.4}$$

where s is the beam size, λ is an indicator to determine the beam shape running from 0 to 1, and ρ is a free parameter to define the beam size. If λ equals 0, $F(x)$ corresponds to Gaussian; If λ equals 1, $F(x)$ corresponds to Sqrt. To determine the ρ value, we consider the beam size definition. The beam line simulation assumes the Sqrt beam shape as described above. The calculated beam size by the simulation corresponds to 2τ in eq. (6.3). For consistency of that, ρ is determined as follows. First, we fit a Sqrt function to $F(x;\lambda;I,x_c,s)$ and obtain the fitting result of $S(x;I',x'_c,\tau')$, I', x'_c and τ' of which are adjusted fitting parameters. Assuming the Sqrt function as a reference, $2\tau'$ is thought to be the beam size of $F(x;\lambda;I,x_c,s)$. Next, ρ is determined so that s equals $2\tau'$. Figure 6.1 shows the calculated ρ values for various λ values. The result of $\rho = 2$ at $\lambda = 1$ is consistent. ρ is also confirmed to be a function of only λ. Figure 6.2 shows examples of the convolution results for various λ values. No significant difference of the shape is found in the range of $\lambda < 0.4$.

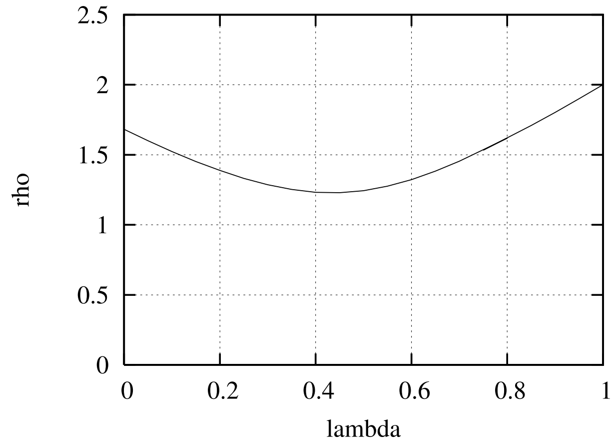

Figure 6.1: ρ vs. λ.

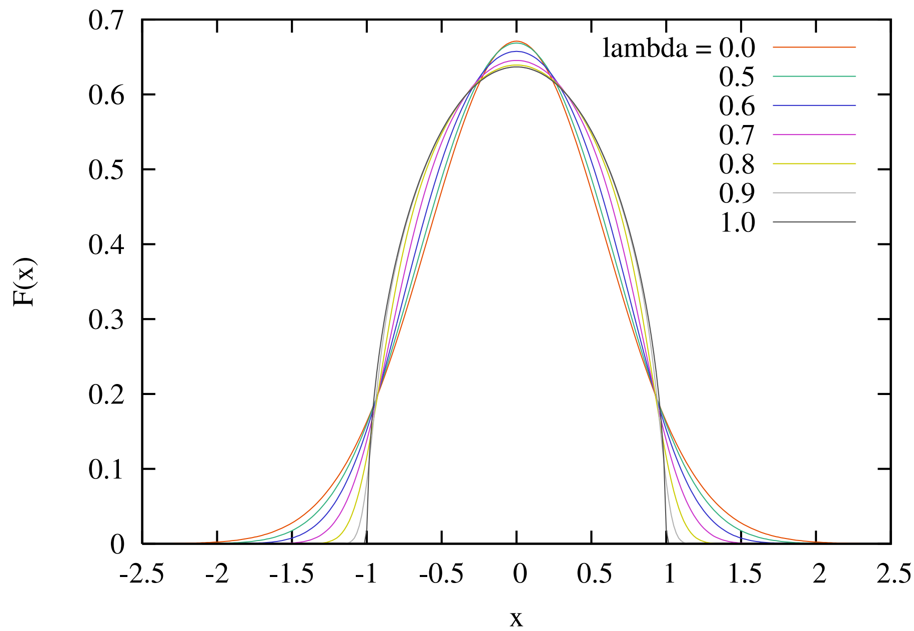

Figure 6.2: Examples of the beam shape $F(x;\lambda;I,x_c,s)$ at various λ values. I,x_c and s is fixed to be 1, 0 and 1, respectively.

“binning error” and “other errors”

The cathode of the monitor is segmented to finite strips. This structure distorts the profile. We refer to the error caused by the finite segmentation effect as “binning error” and divide the resolution into “binning error” and “other errors”.

To evaluate the “binning error” and the “other errors” separately, we have three kinds of profiles in the simulation code as follows,

- incident beam profile,
- reconstructed profile without the error sources, and
- reconstructed profile with the error sources,

where the error sources are AE, GD and SF. The difference between the first and the second profile is caused by only the segmentation effect. Therefore, the “binning error” is evaluated comparing the first and the second profiles. The “other errors” is evaluated comparing the second and the third profiles.

The resolution of the monitor is defined as a combination of the “binning error” and the “other errors”. The detailed discussion of the errors and the resolution is described in Section 6.3.

6.2 Parameter tuning

As described in the previous section, we assume three error sources: the alignment error of the cathode strips (AE), the gain deviation of the system (GD) and the statistical fluctuation (SF). Here, we tune these parameters to match the beam test results. The tuning result is summarized in Table 6.1.

To estimate the amount of the error sources, we use the obtained beam profile in the beam test. Here we focus the difference between the obtained profile and the fitted Gaussian shape. The difference should reflect the resolution deterioration factors, the finite cathode segmentation and the three error sources. Figure 6.3 shows the difference. The red points and the green ones in the left plot correspond to the two monitors, “ssem1” and “ssem2”, respectively. Correlation between “ssem1” and “ssem2” can be seen, and both ”ssem1” and ”ssem2” have the systematic difference from the Gaussian fitting shape around $-10 < x <$ 10 mm region. This difference show that the beam shape at NML is not exactly Gaussian. To extract the effect of the deterioration factors, the difference between the red points and the green ones is plotted as shown in the right side in the figure. There are significant difference around the beam center but little difference at the both sides of the plot. Here we expect the error sources SF to make the uniform difference in the plot, while GD to make the difference around the beam center. Then we consider that SF is negligible by comparing the GD, and we assume SF to be 0 in the simulation. Small SF indicates that the SSEM resolution is mostly determined by the systematic error sources. The resolution stability for small finite SF is also confirmed.

In fabrication of the prototype SSEM, the cathode strips are aligned by hand. We will also do the same way for J-PARC SSEM. Therefore, the alignment error of several ten μm is thought to arise. We assume the error of 50μm as one sigma of Gaussian distribution.

The remaining parameter to be determined is GD. We adjust it so that the simulation reproduces the beam test results. According to the beam test, the beam position difference between "ssem1" and "ssem2" has deviation of 0.07mm, and the beam size difference also has deviation of 1.8%. On the other hand, the simulation with 50μm AE, 2% GD and 0 SF presents the position deviation of 0.066mm and the size deviation of 2.0%, which are consistent with the beam test results. Figure 6.4 shows examples of the reproduced plots, which correspond to Figure 5.20 and 5.21. We fix the GD value to be 2% in the simulation. In addition, the stability of the GD value against the AE variation is also confirmed. If we change the AE in the range of 0.00-0.08mm, the GD value is obtained to be in 1.5-2.3%.

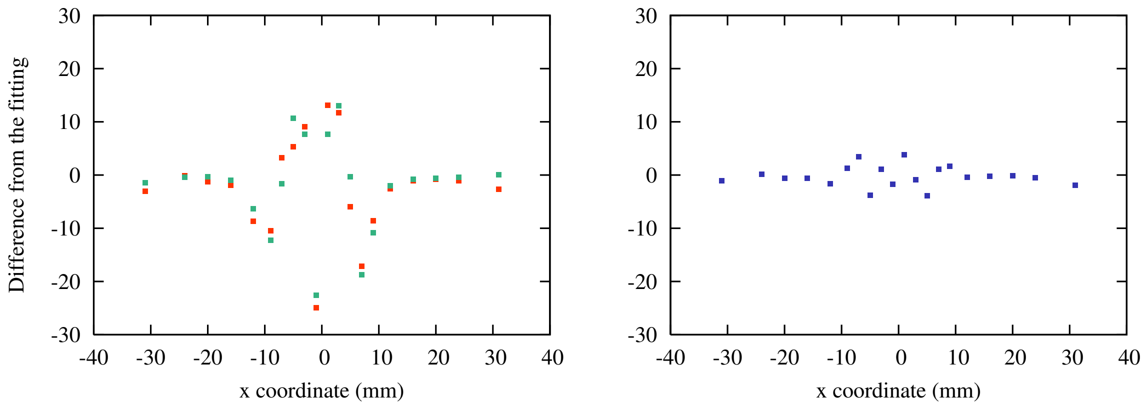

Figure 6.3: Difference from the fitting curve. The red points and green ones in the left plot correspond to "ssem1" and "ssem2" respectively. The blue points in the right plot show the difference between the red points and the green ones in the left plot.

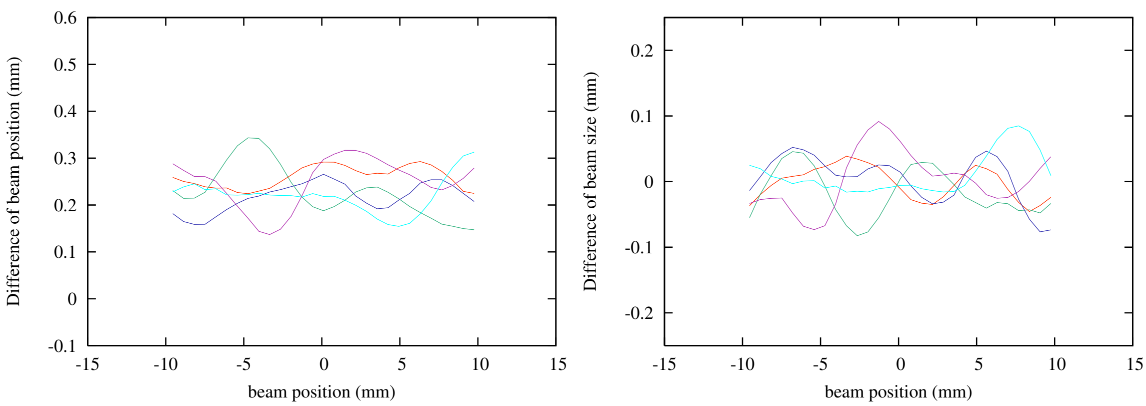

Figure 6.4: Reproduced deviation of the difference between "ssem1" and "ssem2". The left and right plots correspond to the position and size difference, respectively. The different colors correspond to different trial runs.

Alignment error of cathode strips (AE)	50μm (1σ of Gaussian distribution)
Gain deviation of the system (GD)	2% (1σ of Gaussian distribution)
Statistical fluctuation (SF)	non

Table 6.1: Error parameters in the simulation. The parameters are tuned to match the beam test.

6.3 Error characteristics

As described above, the resolution is divided into the "binning error" and the "other errors". In this section, we show characteristics of each error.

Error distributions

In the simulation, the incident beam profile and the cathode design must be fixed first. As an instance, we set them as in Table 6.2. The beam size of 15mm is chosen from the range of the expected beam size, 6-33mm. The cathode design is based on the design template determined in Section 3.3.

Incident beam profile	Beam shape (λ)	0.7
	Beam size	15
Cathode design	Strip width	2mm
	Strip spacing	1mm
	# of strips	22

Table 6.2: Beam profile and cathode design parameters in the simulation.

The calculated distribution of the "binning error" is shown in Figure 6.5. The left and right plots show the position and size error, respectively. Here the incident beam position is artificially fluctuated by the strip pitch (3mm) near the center of the monitor, and the beam size is also fluctuated by a half of the strip pitch (1.5mm). The fluctuation follows a flat distribution, and beam position and size are in the ranges of -1.5-1.5mm and 14.25-15.75mm, respectively. These fluctuations are determined based on the periodic changes of the binning errors on the beam position and size, which are caused by the structural symmetry of the cathode design. In the figure, the shape of the error distribution looks Gaussian for the position error but non-Gaussian for the size error. As a matter of fact, it is confirmed that the distribution of the position error also becomes non-Gaussian for large λ (> 0.9). To obtain a representative of the "binning error", we extract the root value of the square sum of the errors, which corresponds to the rms value calculated assuming the zero mean. For convenience, we refer to this representative value as "binning rms". In the current case, the binning rms is obtained to be 1.0×10^{-5}mm for the position error and 0.021mm(0.14%) for the size error.

The distribution of the "other errors" is shown in Figure 6.6. The left and right plots show the position and size errors, respectively. The distributions are obtained assuming the finite error sources, the amounts of which are determined in the previous section. In the figure, the shape of the both distributions looks like Gaussian. This feature is confirmed under various conditions. As a representative of the "other errors", we use the root value of the square sum and refer to it as “other rms” in the same way as the binning rms. In this case, the ”other rms” is obtained to be 0.054mm for the position error or 0.068mm(0.45%) for the size error.

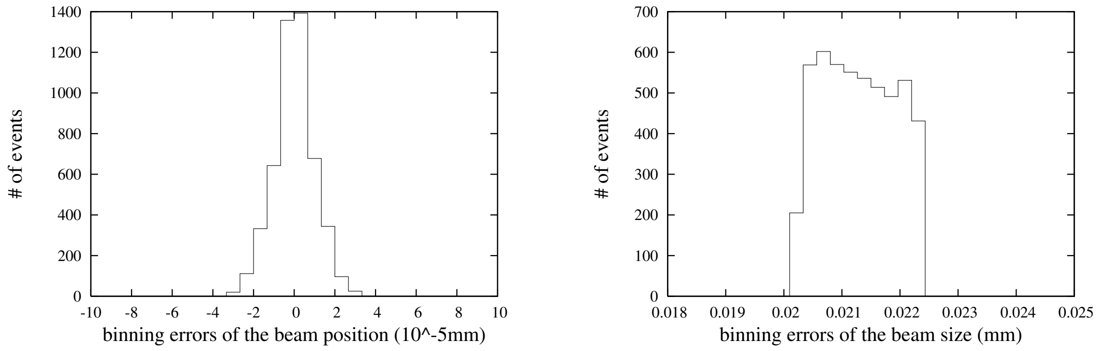

Figure 6.5: Distribution of the binning error at $\lambda = 0.7$.

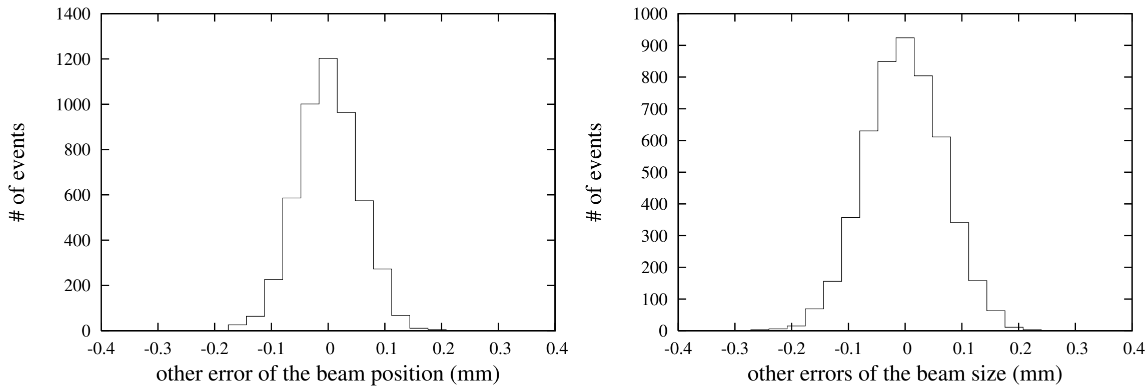

Figure 6.6: Distribution of the other error at $\lambda = 0.7$.

Dependence on the beam shape

To understand the behavior of the error, we investigate the dependence of the error on the beam shape. The simulation setting is the same as in Table 6.2 except for the beam shape parameter λ.

The dependence of the “binning error” on the beam shape is shown in Figure 6.7. The binning rms is plotted for various λ values. In both the position error and the size one, drastic increase can be seen in the back of $\lambda = 0.8$. This tendency is confirmed in common under the realistic conditions; an exception is, for example, the case of too large beam size for the coverage of the cathode. This is thought to be caused by sharp edges of the Sqrt function.

The dependence of the other rms is also confirmed. Figure 6.8 shows the other rms for λ. In the figure, Sqrt shows good performance compared to Gaussian differently from the binning rms.

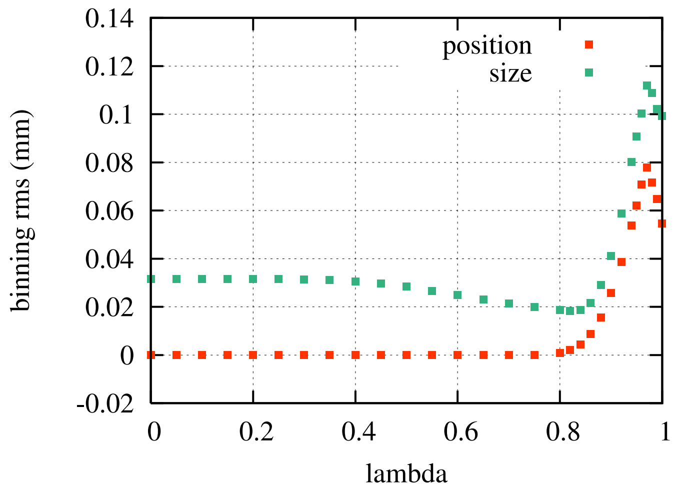

Figure 6.7: Dependence of the ”binning rms” on the beam shape.

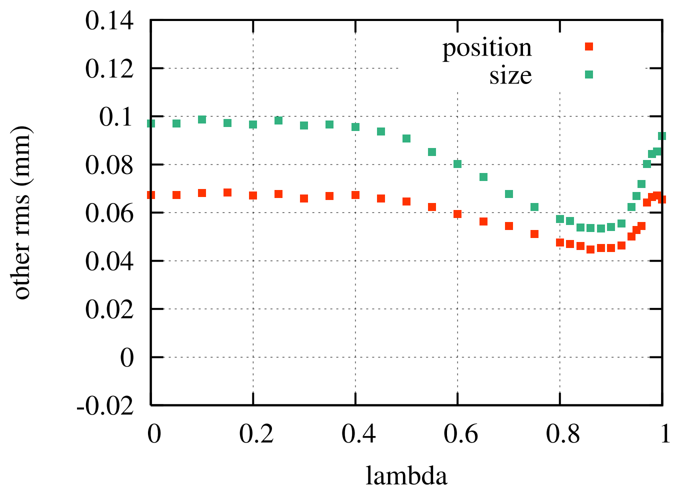

Figure 6.8: Dependence of the ”other rms” on the beam shape.

Dependence on the beam size

Here we check the dependence of the error on the beam size. The assumed cathode design in the simulation is the same as in Table 6.2.

The dependence of the “binning error” on the beam size is shown in Figure 6.9. The binning rms is plotted vs. the beam size at various λ values: 0.0, 0.7, 0.80, 0.90, 0.95, and 1.00. In the figure, the worse errors are found for the larger beam size and for the larger λ value. This tendency is thought to arise from the relative fineness of the cathode segmentation for the beam profile.

The dependence of the “other errors” on the beam size is shown in Figure 6.10. The other rms is plotted vs. the beam size at various λ values: 0.0, 0.7, 0.80, 0.90, 0.95, and 1.00. We find the worse error for the larger beam size. The left figure shows that dependence of the position errors on the beam size and shape is relatively small.

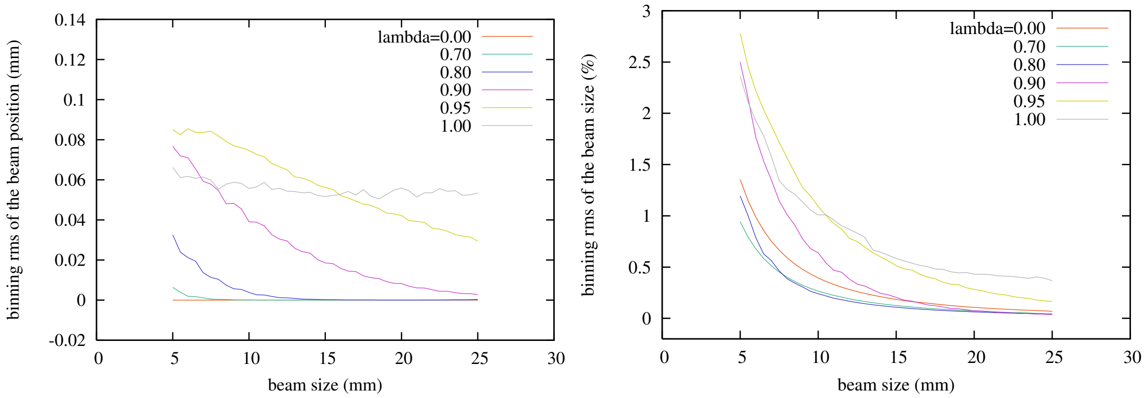

Figure 6.9: Dependence of the ”binning rms” on the beam size. The left and right plot shows the position error and the size one, respectively.

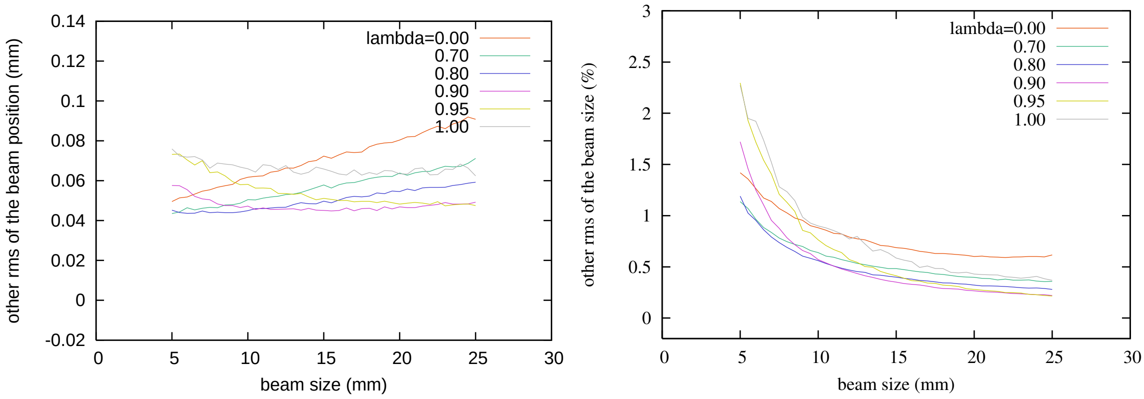

Figure 6.10: Dependence of the ”other rms” on the beam size. The left and right plot shows the position error and the size one, respectively.

Resolution

As the total resolution of the monitor, we take the square mean of the binning rms and the other rms.Here we must note that the binning error becomes dominant for the non-Gaussian distribution case of $\lambda > 0.9$.

6.4 Resolution of the prototype SSEM

The definition of the resolution components is described in the previous section. Then we carry out the simulation under the beam test condition and evaluate the resolution of the prototype SSEM.

The simulation parameter setting is summarized in Table 6.3. The incident beam profile and the cathode design are determined based on the beam test set up.

Incident beam profile	Beam shape (λ)	0 (Gaussian)
	Beam size	6mm
Cathode design	As shown in Figure 5.3	

Table 6.3: Simulation setting.

The simulation results are summarized in Table 6.4. The position resolution of 0.07mm and the size resolution of 1.8% are estimated, and these are better than those estimated in the previous chapter.

	Binning rms	Other rms	Resolution
Beam position (mm)	7.8×10^{-4}	0.040	0.040
Beam size (%)	0.36	0.95	1.0

Table 6.4: Estimated resolutions under the beam test condition.

6.5 Resolution of J-PARC SSEM

The cathode design is determined to suit for the J-PARC neutrino beam line in Section 3.3. The design has 22 strips with uniform strip width and spacing to measure the beam profile, and 2 large strips to detect the beam halo. The strip spacing is fixed to be 1mm, and therefore the strip width is the only parameter to change the cathode design. The adoption of the strip width is shown in Table 3.1. This adoption is determined to satisfy a condition that all monitors in the beam-size range to cover at least twice region of the beam size. Here we evaluate the resolutions for that cathode design and compare them with the requirements.

Figure 6.11-6.15 shows the simulation results. Figure 6.11, 6.12, 6.13, 6.14 and 6.15 correspond to the strip width of 1mm, 2mm, 3mm, 4mm and 5mm, respectively. In all plots, the resolution is plotted vs. the beam size at various λ values: 0.0, 0.7, 0.8, 0.9, 0.95, and 1.0. The range of the beam size in each figure is determined based on Table 3.1. In any case, it is confirmed that the obtained resolutions satisfy the requirements: the position resolution of 0.25mm and the size resolution of 3.5%. We thus conclude that SSEM can provide the required performance under the most realistic conditions: $\lambda < 0.9$. In the case of $\lambda > 0.9$, which corresponds to the beam shape extremely close to Sqrt, there is a concern that the resolution follows a non-Gaussian distribution, and so the obtained resolutions cannot be compared to the requirements strictly. To study this non-Gaussian case in detail, other beamline simulations must be carried out.

6.6 Summary of the simulation study

To study the SSEM performance under the various conditions, we carry out the simulation. We assume the finite cathode segmentation and three error sources as the determinant

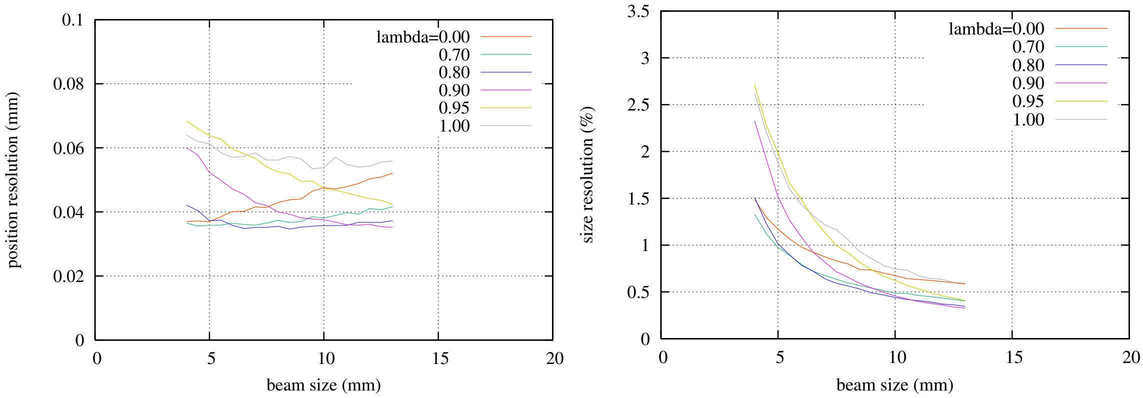

Figure 6.11: Estimated resolution of J-PARC SSEM with 1mm strips.

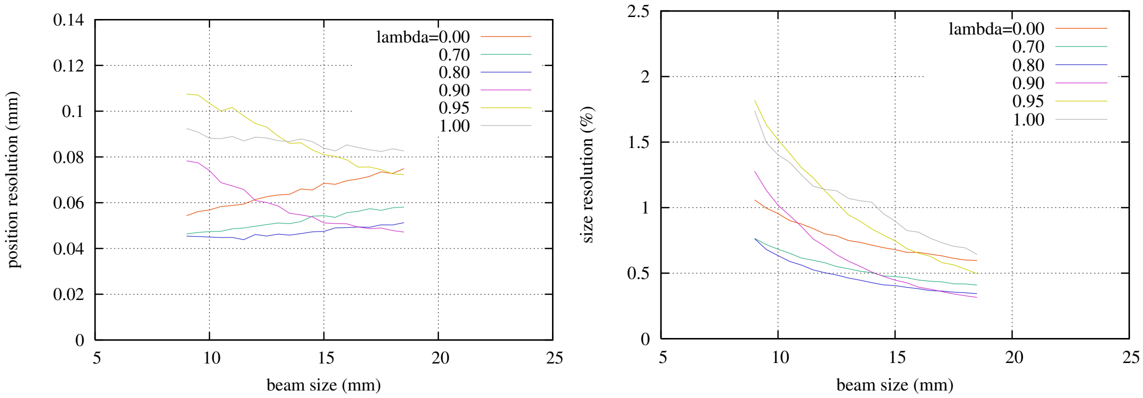

Figure 6.12: Estimated resolution of J-PARC SSEM with 2mm strips.

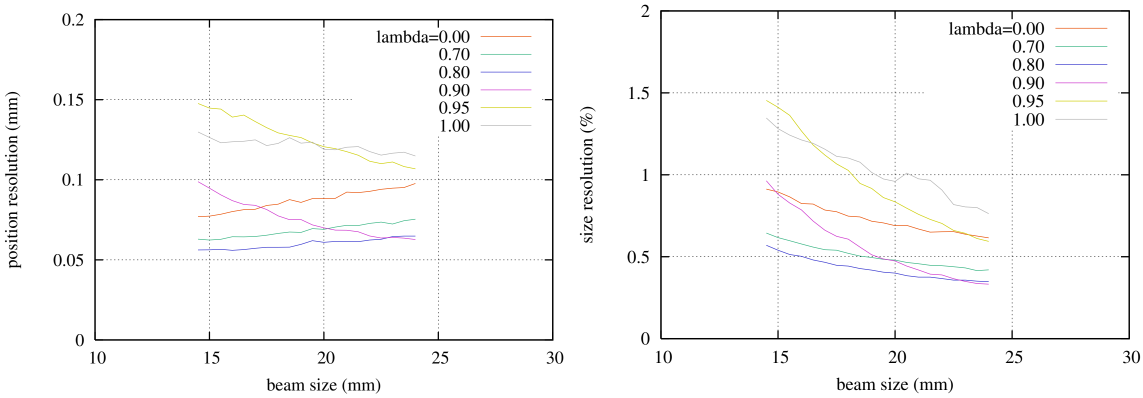

Figure 6.13: Estimated resolution of J-PARC SSEM with 3mm strips.

factors of the resolution. The three error sources are the alignment error of the strips (AE), the gain deviation (GD), and the statistical fluctuation (SF). These parameters are tuned

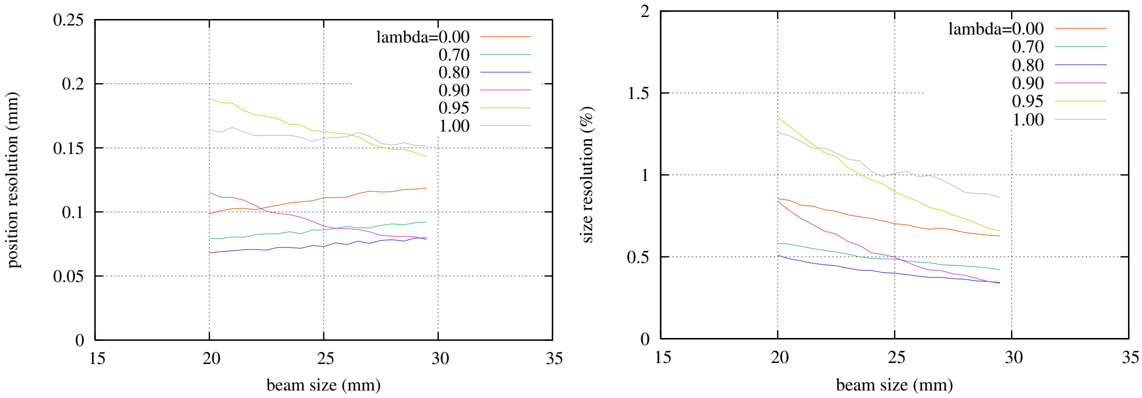

Figure 6.14: Estimated resolution of J-PARC SSEM with 2mm strips.

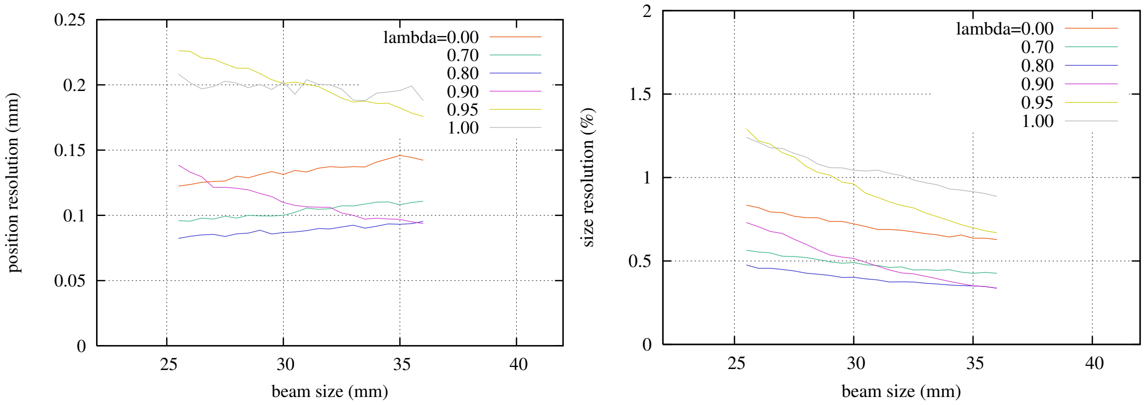

Figure 6.15: Estimated resolution of J-PARC SSEM with 2mm strips.

to match the beam test results. As a result, SF is confirmed to be zero, which indicates that the SSEM resolution is mostly determined by the systematic sources. The resolution is divided into "binning error" and "other errors", which arise from the finite cathode segmentation and the assumed error sources, respectively. The expected beam shape at J-PARC is obtained by the convolution between Gaussian and Sqrt. The beam shape is changed from Gaussian to Sqrt by the beam shape parameter λ running from 0 to 1.

The error characteristics are studied separately for the "binning error" and the "other errors". The error distribution and dependence on the incident beam profile are examined, and we obtain "binning rms" and "other rms" as representatives of those errors. The total monitor resolution is provided by the the sqrt mean of the binning rms and the other rms.

Under the above assumption, we evaluate the resolution of the prototype SSEM; the position resolution of 0.040mm and the size resolution of 1.0%. We also evaluate the resolution of J-PARC SSEM, where the cathode design is determined in Section 3.3. By the evaluation, it is confirmed that the resolution of J-PARC SSEM satisfies the requirements under the most realistic conditions of $\lambda < 0.9$, here the beam shape is not extremely close to Sqrt.

Chapter 7

Summary

We have developed a Segmented Secondary Emission Monitor (SSEM) as a beam profile monitor for the T2K experiment.

The requirements for SSEM are:

- Beam size resolution of better than 3.5%;
- Beam position resolution of ~ 0.25mm;
- Long term gain stability;
- Radiation hardness;
- Need to be equipped with moving mechanism with 0.1mm positioning accuracy; and
- Proper performance under cryogenic temperature of ~ 80K.

We have developed SSEM to satisfy the above requirements.

To check the basic performance of SSEM, we construct a prototype of SSEM and carry out a beam test in the NML beam line in KEK. The obtained beam profiles are consistent with a reference monitor originally equipped in the NML beam line. The secondary emission efficiency is confirmed to be 3.3%, which is consistent with several preceding experiments. The long term stability of the efficiency is also checked and is expected to be sufficient for the J-PARC T2K experiment comparing our result with the CERN SPS result.

Based on the beam test results, we carry out simulation studies and estimate position and size resolutions of SSEM. In the simulation, we assume the finite segmentation of the cathode and three kinds of the error sources as the determinant factors of the resolution: the alignment error of the strips (AE), the gain deviation (GD), and the statistical fluctuation (SF). Those errors are tuned to match the beam test results. As a result of the simulation, the resolution of the prototype monitor used for the beam test is estimated to be 0.040mm (position resolution) and 1.0% (size resolution). The resolutions for the T2K experiment are also estimated, and expected to be better than the requirements.

We design the equipments of SSEM and readout devices. The cathode segmentation is determined to satisfy a condition that all monitors to cover at least twice region of the beam size. As the readout devices, an attenuator module, ADC65 and COPPER are chosen. The circuit design of the attenuator module is fixed and the performance of it is investigated using a handmade prototype. The linearity has turned out to be better than 0.25%. The time constant of shapers on ADC65 is optimized to obtain bunch-by-bunch beam profiles. We make ADC modules with different time constants and evaluate the deterioration of the pulse height precision. Thereby, 50-350nsec are confirmed to be suitable for the J-PARC condition. To fix the specification, 50nsec is chosen because the shorter time constant better conserves the original signal shape.

We carry out cryogenic and irradiation tests. To examine the positioning accuracy of the moving mechanism, we have constructed a test bench and carried out 20,000 shuttle operations so far. By this examination, the accuracy is confirmed to be 0.1mm.

Acknowledgement

I would like to express my great thanks to my supervisor H.Aihara. I am especially thankful to M.Iwasaki and H.Kakuno. I also show my appreciation to T.Abe and T.Uchida.

I greatly acknowledge J-PARC Neutrino Beam Monitor Group: T.Kobayashi, Y.Fujii, A.Ichikawa, Y.Hayato and all the other members. I especially thank KEK Online-electronics group: M.Tanaka, M.Saito, Y.Igarashi and all the other members. I am grateful NML Beamline Group: H.Fujimori, Y.Hashimoto, S.Muto.

I am thankful to N.Hastings, A.Kusaka, K.Tanabe, H.Nakayama, Y.Nakahama for their special support.

Bibliography

[1] Super-Kamiokande collaboration "Evidence for Oscillation of Atmospheric Neutrinos" *Phys.Rev.Lett.* 81,1562 (1998)

[2] The K2K collaboration "Indication of Neutrino Oscillation in a 250km Long-baseline Experiment" *Phys.Rev.Lett.* 90,041801 (2003)

[3] "New MINOS Results on nu Oscillations", http://fpcp2006.triumf.ca/ (2006)

[4] MINOS collaboration "Observation of muon neutrino disappearance with the MINOS detectors in the NuMI neutrino beam", hep-ex/0607088 (2006)

[5] Y.Itow *et al.*, "The JHF-Kamioka neutrino project", hep-ex/010619 (2001)

[6] "Letter Of Intent, Neutrino Oscillation Experiment at JHF", http://neutrino.kek.jp/jhfnu (2003)

[7] Y.Fukuda *et al.* (Super-Kamiokande collaboration), "Evidence for Oscillation of Atmospheric Neutrinos" *Phys. Rev. Lett.* 81,1562 (1998)

[8] Super-Kamiokande collaboration "Tau Neutrinos Flavored over Sterile Neutrinos in Atmospheric Muon Neutrino Oscillations" *Phys.Rev.Lett.* 85,3999 (2000)

[9] Super-Kamiokande collaboration "Solar ^{8}B and hep Neutrino Measurement from 1258 Days of Super-Kamiokande Data" *Phys.Rev.Lett.* 86,5651 (2001)

[10] K.Tanabe Master Thesis (2004)

[11] A.Kusaka Master Thesis (2004)

[12] R.Ishida Master Thesis (2005)

[13] S.A.Blankenburg, *et al. Nuclear Instruments and Methods* **39** (1966), 303; *IEEE Transactions on Nuclear Science* **12** (1965), 935

[14] J.Gamas *et al. CERN SL* 95-62 (1995)

[15] V.Agoritsas *CERN-MPS/Int.CO* 66-30 (1966))

[16] A.R.BERDOZ *et al. TRI-PP* 91-6 (1991); *Nuclear Instruments and Methods A* **302**,26 (1991)

[17] M.Ieiri *et al.* "Response of KEK Secondary Emission Chamber to Several GeV Protons and Deuterons", The 9th Symp. on Acc. Sci. Tech., Tsukuba, Japan (1993)

[18] V.Agoritsas *IEEE Transactions on Nuclear Science* Vol.NS-**26** (1979)

[19] G.Ferioli *CERN SL* 97-71 (1997)